Inertialess Swimming and Propulsion of Slender Bodies

by

Zhiwei Peng

B.Sc., Beijing University of Aeronautics & Astronautics, 2014

A THESIS SUBMITTED IN PARTIAL FULFILLMENT OF
THE REQUIREMENTS FOR THE DEGREE OF

MASTER OF APPLIED SCIENCE

in

The Faculty of Graduate and Postdoctoral Studies

(Mechanical Engineering)

THE UNIVERSITY OF BRITISH COLUMBIA

(Vancouver)

April 2016

Abstract

In this thesis, two problems relevant to the biological locomotion in inertialess environments are studied, one is the characteristics of undulatory locomotion in granular media, the other is the optimal flexibility of a driven microfilament in a viscous fluid.

Undulatory locomotion is ubiquitous in nature and observed in different media, from the swimming of flagellated microorganisms in biological fluids, to the slithering of snakes on land, or the locomotion of sandfish lizards in sand. Despite the similarity in the undulating pattern, the swimming characteristics depend on the rheological properties of different media. Analysis of locomotion in granular materials is relatively less developed compared with fluids partially due to a lack of validated force models but recently a resistive force theory in granular media has been proposed and shown useful in studying the locomotion of a sand-swimming lizard. In this work, we employ the proposed model to investigate the swimming characteristics of a slender filament, of both finite and infinite length, undulating in a granular medium and compare the results with swimming in viscous fluids. In particular, we characterize the effects of drifting and pitching in terms of propulsion speed and efficiency for a finite sinusoidal swimmer. We also find that, similar to Lighthill's results using resistive force theory in viscous fluids, the sawtooth swimmer is the optimal waveform for propulsion speed at a given power consumption in granular media.

Though it is understood that flexibility can improve the propulsive performance of a filament in a viscous fluid, the flexibility distribution that generates optimal propulsion remains largely unexplored. In this work, we employ the resistive force theory combined with the Euler-Bernoulli beam model to examine the optimal flexibility of a boundary driven filament in the small oscillation amplitude limit. We show that the optimality qualitatively depends on the boundary actuation. For large amplitude actuation, our numerics show that complex asymmetry in the waveforms emerge. The results complement our understanding of inertialess locomotion and provide insights into the effective design of locomotive systems in various environments.

Preface

The research presented in this thesis is original work of the thesis author under the supervision of Professor Gwynn J. Elfring in collaboration with Professor On Shun Pak (Santa Clara University, USA).

A version of Chapter 2 was presented at the American Physical Society 68th Annual Division of Fluid Dynamics Meeting (Boston, MA, November 22-24, 2015) by the thesis author and published in *Physics of Fluids*. Z. Peng, O.S. Pak, G.J. Elfring (2016) Characteristics of undulatory locomotion in granular media, Phys. Fluids, 28, 031901.

Chapters 3 and 4 are original, unpublished work of the thesis author.

Table of Contents

List of Tables

List of Figures

Acknowledgements

First of all, I would like to thank my thesis advisor, Gwynn Elfring and my collaborator and mentor On Shun Pak, for being awesome and inspiring. I feel very lucky to have the chance to work with them. I thank Gwynn and On Shun for guidance and encouragement throughout the journey of my research at UBC.

I have been very fortunate to be surrounded by wonderful and talented colleagues, from whom I learned a lot both academically and personally. I would like to thank my lab mates, Gaurav, Babak, Charu and Silvia for being brilliant and supportive. Initially, Gaurav and I were sharing an office in the Rusty Hut, which indeed is a rusty box. Luckily enough, we moved out to a new lab where all the group members have been creating glorious work in the Elfring Alley.

Finally, I would like to thank my friends and family without whose support I could not have made this far.

Dedication

To my parents, for their love and support.

Chapter 1

Introduction

1.1 Swimming at low Reynolds number

Biological locomotion in fluids is ubiquitous in nature and spans a wide range of length scales from the undulatory locomotion of flagellated bacteria in a microscopic world to the swimming of sharks in the vast ocean. It plays a crucial role in predation, avoiding predators or reproduction throughout the whole lifespan of a swimming animal [1]. Biological locomotion in fluids have received substantial attention from biologists, engineers and mathematicians alike in recent decades, among which the study of locomotion at small scales relevant to bacteria or flagella remains more recent [2, 3].

The physics governing locomotion in fluids at small scales are qualitatively different from those of the mesoscale or macroscale locomotion. For swimming bacteria or flagella, inertia plays a negligible role while viscous forces dominate. In general, the motion of a Newtonian fluid is governed by the Navier-Stokes equation,

$$\rho\left(\frac{\partial \mathbf{u}}{\partial t} + \mathbf{u}\cdot\nabla\mathbf{u}\right) = -\nabla p + \mu\nabla^2\mathbf{u} \tag{1.1}$$

where $\mathbf{u}(\mathbf{x}, t)$ is the velocity of the fluid at $\mathbf{x}$ in space and time t, μ is the viscosity of the fluid, ρ is the density of the fluid and p is the pressure. If we non-dimensionalize the Navier-Stokes equations with respect to a characteristic length scale of the microorganism L and a characteristic velocity scale U_0, we have the dimensionless equation given by

$$\mathrm{Re}\left(\frac{\partial \mathbf{u}}{\partial t} + \mathbf{u}\cdot\nabla\mathbf{u}\right) = -\nabla p + \nabla^2\mathbf{u} \tag{1.2}$$

where the same variables as the dimensional ones are used and

$$\mathrm{Re} = \frac{\rho U_0 L}{\mu} \tag{1.3}$$

is the Reynolds number which compares the relative importance of inertia effects to viscous forces. For a typical microorganism such as *E. Coli* ($U_0 \approx 30\mu\mathrm{m}/s$, $L \approx 10\mu\mathrm{m}$) swimming in water, the Reynolds number is on the order of 3×10^{-4} and thus negligible [4]. In the mathematical limit of zero Reynolds number, we have the Stokes equations governing the motion

of a fluid,

$$-\nabla p + \nabla^2 \mathbf{u} = 0, \quad \nabla \cdot \mathbf{u} = 0. \tag{1.4}$$

The linearity and time independence of the Stokes equations leads to kinematic reversibility, which is well-described by Purcell's famous "scallop theorem" states that a reciprocal motion (a deformation that exhibits time-reversal symmetry) cannot generate any net propulsive thrust [5]. In order to break the constraint of time-reversibility, many microorganisms including flagellated bacteria and spermatozoa achieve self-propulsion by passing deformation waves along their slender flexible bodies [3, 6, 7].

1.2 Slender body hydrodynamics

If the length of a swimming cylindrical body L is much larger than its radius r, $r/L \ll 1$. In this case, instead of solving the Stokes equations in the fluid domain, we can obtain a local drag law, which is the so-called Resistive Force Theory (RFT)[6, 8, 9]. RFT states that the viscous force per unit length on the body at a point is related linearly to the local filament velocity, namely,

$$\mathbf{f}_{\text{vis}} = -\left(\xi_{\perp}\mathbf{nn} + \xi_{\parallel}\mathbf{tt}\right) \cdot \mathbf{x}_t, \tag{1.5}$$

where the hydrodynamics at this order is characterized by the tangential $\xi_{\parallel}$ and normal $\xi_{\perp}$ resistive coefficients, the subscript t indicates differentiation with respect to time and $\mathbf{n}$ and $\mathbf{t}$ are the local unit normal and tangent vectors along the body. For a slender, cylindrical rod, the resistance ratio $\gamma = \xi_{\perp}/\xi_{\parallel} \to 2$ as $L/r \to \infty$. This drag anisotropy ($\gamma \neq 1$) is crucial for locomotion at low Reynolds number [3, 4].

1.3 Thesis outline

This thesis studies the characteristics and optimality in swimming and propulsion of a slender filament in granular media and viscous fluids.

Chapter 2 examines the characteristics of undulatory locomotion of a slender swimmer in granular media and compare the results with those for swimming in a viscous fluid. We characterize the complex kinematics and optimal swimming and discuss the similarities to swimming in viscous fluids.

Chapter 3 presents a mathematical modeling of the propulsion of a filament with nonuniform flexibility along the body under a boundary actuation. We explore the optimal flexibility distribution that maximizes the propulsive force of a driven filament for small amplitude. We note that the optimality qualitatively depends on the boundary actuation, so that one may not extend the results of one case to other cases of propulsion where the actuation might differ.

Chapter 4 investigates the fully nonlinear dynamics of a boundary driven filament using a numerical approach. For small amplitude, we compare the results from numerics to the small amplitude asymptotic solution and observe good agreement between them. For large amplitude, we show that the linear theory breaks down and complex asymmetry in the waveforms emerge. The results complement our understanding of inertialess locomotion and provide insights into the effective design of locomotive systems in various environments.

Chapter 2

Characteristics of undulatory locomotion in granular media[1]

2.1 Introduction

Undulatory locomotion, the self-propulsion of an organism via the passage of deformation waves along its body, is ubiquitous in nature [10, 11]. Flagellated microorganisms swim in fluids [5, 8, 9, 12–14], snakes slither on land [15–18]and sandfish lizards (*Scincus scincus*) undulate in granular substrates [19–21]. Yet the underlying physics differ: from viscous forces [3] in fluids to frictional forces [20] in terrestrial media. The investigation of these undulatory mechanisms in different environments advances our understanding of various biological processes [2, 11] and provides insights into the effective design of biomimetic robots [22, 23].

The swimming of microorganisms in Newtonian fluids, where viscous forces dominate inertial effects, is governed by the Stokes equations [3]. Despite the linearity of the governing equation, locomotion problems typically introduce geometric nonlinearity, making the problem less tractable [24]. For slender bodies such as flagella and cilia, Gray and Hancock [8] exploited their slenderness to develop a local drag model, called resistive force theory (RFT), which has been shown useful in modeling flagellar locomotion and the design of synthetic micro-swimmers [3, 4]. In this local theory, hydrodynamic interactions between different parts of the body are neglected and the viscous force acting on a part of the body depends only on the local velocity relative to the fluid. Using RFT, Lighthill showed that, for an undulating filament of infinite length, the sawtooth waveform is the optimal beating pattern maximizing hydrodynamic efficiency [9].

Locomotion in granular media (GM) is relatively less well understood due to their complex rheological features [25, 26]. The frictional nature of the particles generates a yield stress, a threshold above which the grains flow in response to external forcing [26]. Different from viscous fluids, the resistance experienced by a moving intruder originates from the inhomogeneous and anisotropic response of the granular force chains, which are narrow areas of strained grains surrounded by the unstrained bulk of medium [27]. At low locomotion speed, where the granular matter is in a quasi-static regime, the effect of inertia is negligible compared to frictional and gravitational forces from granular media [21], which is similar to that of a low Reynolds-number

[1] A version of Chapter 2 has been published in *Physics of Fluids*. Peng, Zhiwei, Pak, On Shun and Elfring, Gwynn J., Characteristics of undulatory locomotion in granular media, Phys. Fluids, 28, 031901 (2016)

fluid. In this regime, studies measuring the drag force of an intruder moving through a GM reveal that the drag force is independent of the speed of the intruder, but it increases with the depth of GM and proportional to the size of the intruder [27–31].

Recently, Maladen *et al.* [20] studied the subsurface locomotion of sandfish in dry granular substrates. While the crawling and burying motion of a sandfish is driven by its limbs, an undulatory gait is employed for subsurface locomotion without use of limbs. Using high speed x-ray imaging, the subsurface undulating pattern of the sandfish body was found to be well described by a sinusoidal waveform. A major challenge in the quantitative analysis of locomotion in granular materials is a lack of validated force models like the Stokes equation in viscous fluids [25, 26]. But inspired by the success of RFT for locomotion in viscous fluids, Maladen *et al.* [20] developed an empirical RFT in dry granular substrates for slender bodies (Sec. 2.2.2), which was shown effective in modeling the undulatory subsurface locomotion of sandfish [20]. The proposed force model thus enables theoretical studies to address some fundamental questions on locomotion in granular media. In this paper we employ the proposed RFT to investigate the swimming characteristics of a slender filament of finite and infinite length undulating in a granular medium and compare the results with those in viscous fluids. In particular, previous analysis using the granular RFT considered only force balance in one direction [20] and hence a swimmer can only follow a straight swimming trajectory in this simplified scenario. Here we extend the results by considering a full three-dimensional force and torque balances, resulting in more complex kinematics such as pitching, drifting and reorientation. The swimming performance in relation to these complex kinematics is also discussed.

This chapter is organized as follows. We formulate the problem and review the recently proposed RFT in granular media in Sec. 2.2. Swimmers of infinite length are first considered (Sec. 2.3): we determine that the optimal waveform maximizing swimming efficiency, similar to results in viscous fluids, is a sawtooth (Sec. 2.3.1); we then study the swimming characteristics of sawtooth and sinusoidal swimmers in granular media and compare the results with swimming in viscous fluids (Sec. 2.3.2). Next we consider swimmers of finite length (Sec. 2.4) and characterize the effects of drifting and pitching in terms of propulsion speed and efficiency, before concluding with remarks in Sec. 2.5.

2.2 Mathematical Formulation

2.2.1 Kinematics

We consider an inextensible cylindrical filament of length L and radius r such that $r \ll L$, and assume that it passes a periodic waveform down along the body to propel itself in granular substrates. Following Spagnolie and Lauga [32], the waveform is defined as $\mathbf{X}(s) = [X(s), Y(s), 0]^{\mathsf{T}}$, where $s \in [0, L]$ is the arc length from the tip. The periodicity of the waveform

can then be described as

$$X(s+\Lambda) = X(s) + \lambda, \quad Y(s+\Lambda) = Y(s), \tag{2.1}$$

where λ is the wave length and Λ the corresponding arc length along the body. N is the number of waves passed along the filament. Note that $L = N\Lambda$ and $\lambda = \alpha\Lambda$, where $0 < \alpha < 1$ is due to the bending of the body [32].

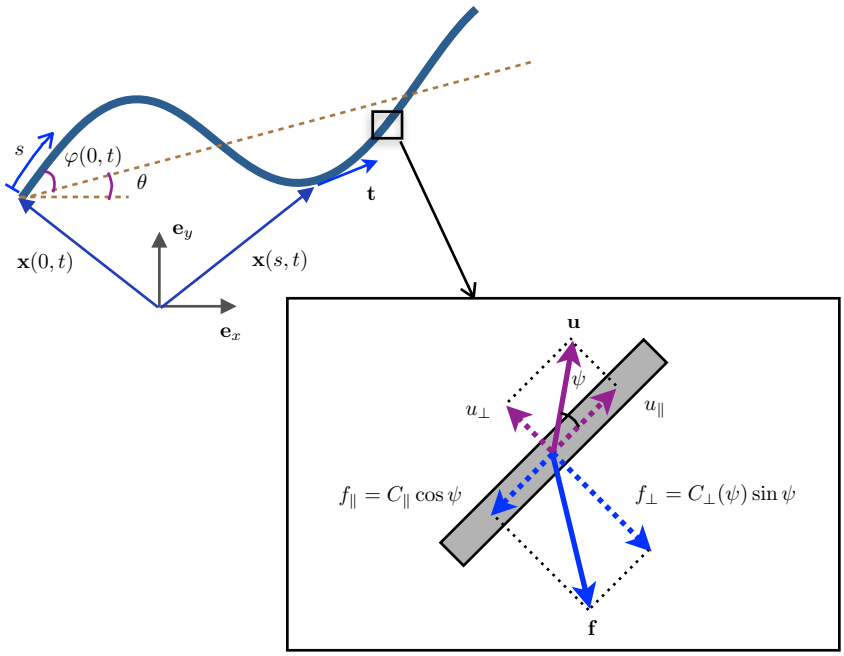

Figure 2.1: Illustration of an undulating slender filament and the resistive force theory in granular media. The body propagates a prescribed waveform to propel itself. Each element $\mathrm{d}s$ experiences a drag force $\mathrm{d}\mathbf{F} = \mathbf{f}\,\mathrm{d}s$. The basis vectors $\{\mathbf{e}_x, \mathbf{e}_y\}$ and the position vectors of its head $\mathbf{x}(0,t)$ and a material point $\mathbf{x}(s,t)$ on the body in the lab frame are shown ($\mathbf{e}_z = \mathbf{e}_x \times \mathbf{e}_y$). The angle between the local velocity $\mathbf{u}$ and unit tangent vector $\mathbf{t}$ is $\psi(s,t)$.

Initially, the filament is oriented along the x-axis of the lab frame with its head at $\mathbf{x}_0$. At time t, the filament is passing the waveform at a phase velocity $\mathbf{V}$ (with constant phase speed V) along the waveform's centerline, which is oriented at an angle $\theta(t)$ to the x-axis (Fig. 2.1). In a reference frame moving with the wave phase velocity $\mathbf{V}$, a material point on the filament is moving tangentially along the body with speed $c = V/\alpha$, and hence the period of the waveform is $T = \lambda/V = \Lambda/c$. By defining the position vector of a material point at location s and time t in the lab frame as $\mathbf{x}(s,t)$, we obtain

$$\mathbf{x}(s,t) - \mathbf{x}(0,t) = \boldsymbol{\Theta}(t) \cdot \mathbf{R}(s,t), \tag{2.2}$$

where

$$\mathbf{\Theta}(t) = \begin{bmatrix} \cos\theta(t) & -\sin\theta(t) & 0 \\ \sin\theta(t) & \cos\theta(t) & 0 \\ 0 & 0 & 1 \end{bmatrix} \tag{2.3}$$

is the rotation matrix, and $\mathbf{R}(s,t) = \mathbf{X}(s,t) - \mathbf{X}(0,t)$, and note that $\mathbf{X}(s,t) = \mathbf{X}(s-ct)$. Then, the velocity of each material point in the lab frame would be

$$\mathbf{u}(s,t) = \dot{\mathbf{x}}(0,t) + \dot{\theta}\mathbf{\Theta}\cdot\mathbf{R}^{\perp} + \mathbf{\Theta}\cdot\dot{\mathbf{R}}, \tag{2.4}$$

where $\mathbf{R}^{\perp} = \mathbf{e}_z \times \mathbf{R}$, and dot denotes time derivative. The unit tangent vector in the direction of increasing s is

$$\mathbf{t} = \mathbf{x}_s = \mathbf{\Theta}\cdot\mathbf{X}_s(s,t), \tag{2.5}$$

where the subscript s denotes the derivative with respect to s. The angle between the local velocity vector $\mathbf{u}$ and the local unit tangent vector $\mathbf{t}$ is ψ:

$$\cos\psi = \hat{\mathbf{u}}\cdot\mathbf{t}, \quad \hat{\mathbf{u}} = \frac{\mathbf{u}}{\|\mathbf{u}\|}. \tag{2.6}$$

Now, to define the waveform we specify the tangent angle made with the centerline of the waveform

$$\varphi(s,t) = \arctan\frac{Y_s}{X_s}, \tag{2.7}$$

or

$$\mathbf{X}_s = [\cos\varphi, \sin\varphi, 0]^{\mathsf{T}}. \tag{2.8}$$

Note that we have the following geometric relations:

$$\mathbf{R} = \int_0^s \mathbf{X}_s\,\mathrm{d}s, \quad \dot{\mathbf{R}} = \int_0^s \dot{\varphi}\mathbf{X}_s^{\perp}\,\mathrm{d}s, \tag{2.9}$$

$$\mathbf{t} = \mathbf{\Theta}\cdot\mathbf{R}_s = \mathbf{\Theta}\cdot\mathbf{X}_s, \tag{2.10}$$

where $\mathbf{X}_s^{\perp} = \mathbf{e}_z \times \mathbf{X}_s$, and

$$\alpha = \frac{\lambda}{\Lambda} = \frac{1}{\Lambda}\int_0^{\Lambda} \cos\varphi\,\mathrm{d}s. \tag{2.11}$$

The inextensibility assumption requires that $\partial[\mathbf{x}_s\cdot\mathbf{x}_s]/\partial t = 0$, and the arc-length parameterization of the swimming filament naturally satisfies this constraint. The tangent angle is specified

as a composition of different Fourier modes[2]:

$$\varphi(s,t) = \sum_{n=1}^{n^*} \left\{ a_n \cos\left[\frac{2\pi n}{\Lambda}(s-ct)\right] + b_n \sin\left[\frac{2\pi n}{\Lambda}(s-ct)\right] \right\}, \tag{2.12}$$

where

$$a_n = \frac{2}{\Lambda}\int_0^{\Lambda} \varphi(s,0)\cos\left[\frac{2\pi n s}{\Lambda}\right] \mathrm{d}s, \tag{2.13}$$

$$b_n = \frac{2}{\Lambda}\int_0^{\Lambda} \varphi(s,0)\sin\left[\frac{2\pi n s}{\Lambda}\right] \mathrm{d}s, \quad n = 1,2,3,... \tag{2.14}$$

2.2.2 Resistive force theory

In low Reynolds number swimming of a slender filament in a Newtonian fluids, the resistive forces are linearly dependent on the local velocity. The force per unit length exerted by the fluid on the swimmer body at location s and time t is given by

$$\mathbf{f}(s,t) = -K_T \mathbf{u}\cdot\mathbf{tt} - K_N(\mathbf{u} - \mathbf{u}\cdot\mathbf{tt}), \tag{2.15}$$

where K_N and K_T are, respectively, the normal and tangential resistive coefficients. The self-propulsion of elongated filaments is possible because of drag anisotropy ($K_N \neq K_T$). A detailed discussion on this property can be found in the review paper by Lauga and Powers [3]. Recent experimental studies of direct force and motion measurements on undulatory microswimmers in viscous fluids find excellent agreement with RFT predictions [33, 34]. The ratio $r_K = K_N/K_T$ varies with the slenderness (L/r) of the body. In the limit of an infinitely slender body, $L/r \to \infty$, $r_K \to 2$, which is the value adopted in this study.

For undulatory locomotion in dry granular media, we only consider the slow motion regime where grain-grain and grain-swimmer frictional forces dominate material inertial forces [20]. The motion of the swimmer is confined to the horizontal plane such that the change of resistance due to depth is irrelevant. In this regime the granular particles behave like a dense frictional fluid where the material is constantly stirred by the moving swimmer [25]. The frictional force acting tangentially everywhere on the surface of a small cylindrical element is characterized by C_F, which is refered to as the flow resistance coefficient [20]. The other contribution to the resistive forces is the in-plane drag-induced normal force, which is characterized by C_S. Note that C_S is a constant because the drag is independent of the velocity magnitude. The normal resistive coefficient $C_\perp$ depends on the orientation (ψ) of the element with respect to the direction of motion (Fig. 2.1). In other words, the resistive force exerted by the granular

[2]For numerical computations, the number of modes n^* has to be finite. In this chapter, $n^* = 100$ as detailed in Appendix A

material on the swimmer per unit length

$$\mathbf{f}(s,t) = -C_{\parallel}\hat{\mathbf{u}}\cdot\mathbf{tt} - C_{\perp}(\hat{\mathbf{u}} - \hat{\mathbf{u}}\cdot\mathbf{tt}), \tag{2.16}$$

where

$$C_{\parallel} = 2rC_F, \tag{2.17}$$

$$C_{\perp}(\psi) = 2rC_F + \frac{2rC_S\sin\beta_0}{\sin\psi} = C_{\parallel}\left(1 + \frac{C_S\sin\beta_0}{C_F\sin\psi}\right), \tag{2.18}$$

$\tan\beta_0 = \cot\gamma_0\sin\psi$ and γ_0 is a constant related to the internal slip angle of the granular media[20]. Although a complete physical picture of the dependence of $C_\perp$ on the orientation ψ remains elusive, the application of the granular RFT proves to be effective. Several studies have applied the granular RFT to study the locomotion of sand-swimming animals and artificial swimmers and found good agreement with experiments and numerical simulations [23, 25]. A detailed discussion about the effectiveness of granular RFT on modelling sand-swimming can be found in a review article by Zhang and Goldman [25].

An important parameter characterizing the response of dry GM to intrusion is the volume fraction ϕ, which is defined as the ratio of the total volume of the particles divided by the occupied volume. The level of compaction affects drag response as closely packed (high ϕ) GM expands to flow while loosely packed (low ϕ) material would consolidate [20]. The drag parameters C_S, C_F and γ_0 depend on the volume fraction of the GM. In our study, we refer to the GM with $\phi = 0.58$ as loosely packed (LP) whereas $\phi = 0.62$ as closely packed (CP). The numerical values of the drag parameters are adopted from the paper by Maladen *et al.* [20], where the forces at a fixed depth of 7.62 cm were measured by towing a cylinder of stainless steel. The drag parameters are presented in Table 2.1.

Packing	ϕ	C_S, N/m^2 $\times 10^{-4}$	C_F, N/m^2 $\times 10^{-4}$	γ_0,degree
LP	0.58	0.51	0.28	13.84
CP	0.62	0.77	0.59	12.21

Table 2.1: The parameters of the resistive force model in LP and CP GM as obtained by Maladen *et al.* [20]

Without external forcing, the self-propelled filament satisfies force-free and torque-free conditions:

$$\mathbf{F} = \int_0^L \mathbf{f}(s,t)\,\mathrm{d}s = \mathbf{0}, \tag{2.19}$$

$$\mathbf{T} = \int_0^L [\mathbf{x}(s,t) - \mathbf{x}(0,t)] \times \mathbf{f}(s,t)\,\mathrm{d}s = \mathbf{0}. \tag{2.20}$$

The granular RFT exhibits the symmetry property that $\mathbf{u} \to -\mathbf{u}$ results in $\mathbf{f} \to -\mathbf{f}$. Com-

bining this symmetry with the kinematics of the undulatory locomotion (see Sec. 2.2.1), one can show that the velocities $-\dot{\mathbf{x}}(0,t)$ and $-\dot{\theta}$ are solutions to the instantaneous motion under a reversal of the actuation direction ($c \to -c$) provided that $\dot{\mathbf{x}}(0,t)$ and $\dot{\theta}$ are solutions to the original problem (without reversal of the actuation). This symmetry is of course present in viscous RFT and this commonality, as we shall show, leads to qualitatively similar swimming behaviors.

2.2.3 Swimming efficiency

The instantaneous swimming speed of the filament is given by $\dot{\mathbf{x}}(0,t)$, and the mean swimming velocity is defined as $\mathbf{U} = \langle \dot{\mathbf{x}}(0,t) \rangle = U_x \mathbf{e}_x + U_y \mathbf{e}_y$ with the magnitude $U = \|\mathbf{U}\|$. The angle brackets $\langle ... \rangle$ denote time-averaging over one period T. The efficiency of the undulatory locomotion for a given deformation wave is defined by the ratio of the power required to drag the straightened filament through the surrounding substance to the power spent to propel the undulating body at the same velocity [35]. Hence, the efficiency for undulatory swimming of slender filaments in viscous fluid (η_f) and granular substance (η_g), respectively, are

$$\eta_f = \frac{K_T L U^2}{P}, \quad \eta_g = \frac{C_\parallel L U}{P}, \tag{2.21}$$

where

$$P = \left\langle \int_0^L \mathbf{f}(s,t) \cdot \mathbf{u}(s,t)\, \mathrm{d}s \right\rangle. \tag{2.22}$$

The optimal swimming can then be interpreted as either swimming with the maximum speed at a given power or swimming with the minimum power at a given speed.

2.2.4 Waveforms

We consider two typical planar waveforms that have been well studied in Newtonian swimming: the sinusoidal waveform, and the sawtooth waveform (Fig. 2.2). The sinusoidal waveform can be described by its Cartesian coordinates[3]:

$$Y = b \sin k(X + X_0), \tag{2.23}$$

where $k = 2\pi/\lambda$ is the wave number, kX_0 is the initial phase angle of the waveform, and b the wave amplitude. The dimensionless wave amplitude is defined as $\epsilon = kb$.

The sawtooth waveform, which consists of straight links with a bending angle β ($\varphi = \pm\beta/2$),

[3]The local tangent $\varphi(s,t)$ of the Cartesian sine can be obtained using the relation $\mathrm{d}s = \sqrt{1 + Y_X^2}\, \mathrm{d}X$ combined with Eq. (2.7). Then we obtain the Fourier coefficients of the Cartesian sine using *fsolve* because the functions are nonlinear.

can be described as

$$Y = \frac{2b}{\pi} \arcsin[\sin k(X + X_0)], \tag{2.24}$$

The dimensionless amplitude $\epsilon = kb = (\pi/2)\tan(\beta/2)$.

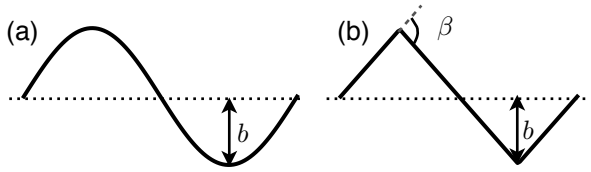

Figure 2.2: Undulating filaments with a single wave ($N = 1$). (a): sinusoid, $kX_0 = 0$; (b) sawtooth, $kX_0 = 0$

2.3 Bodies of infinite length

For bodies of infinite length ($L \to \infty$), the swimming motion is steady and unidirectional, and hence $\dot{\theta(t)} = 0$. Without loss of generality, we assume the filament propagates the deformation wave in the positive x-direction. Then the velocity of a material point on the body can be written as

$$\mathbf{u} = -U\mathbf{e}_x + V\mathbf{e}_x - c\mathbf{t}, \tag{2.25}$$

where U is the swimming speed [35]. For an infinite swimmer, the unidirectional swimming velocity for a given waveform can be obtained from only the force balance in the x-direction, $\mathbf{F} \cdot \mathbf{e}_x = 0$, over a single wavelength,

$$\int_0^\Lambda \left(\frac{C_S \sin\beta_0}{\sin\psi} + C_F \right) \hat{\mathbf{u}} \cdot \mathbf{e}_x \, \mathrm{d}s - \int_0^\Lambda \frac{C_S \sin\beta_0}{\sin\psi} (\hat{\mathbf{u}} \cdot \mathbf{t})\mathbf{t} \cdot \mathbf{e}_x \, \mathrm{d}s = 0. \tag{2.26}$$

The above integral equation can be solved for U numerically for a given waveform in general but is analytically tractable in certain asymptotic regimes, which we discuss below.

2.3.1 Optimal shape: numerical results

A natural question for swimming organisms is how their swimming gaits evolve under the pressure of natural selection [36], since being able to swim does not necessarily mean one does it efficiently. The understanding of optimal swimming may reveal nature's design principles and guide the engineering of robots capable of efficient self-propulsion. As a response, the optimal strategies of several Newtonian swimming configurations have been studied. Becker *et al.*[37] determined the optimal strategy of Purcell's three-link swimmer under constant forcing and

minimum mechanical work. Tam and Hosoi [38] improved the swimming speed and efficiency of the optimal strategy of Purcell's three-link swimmer by allowing simultaneous rather than sequential movement of both hinges (kinematic optimization). Using viscous RFT, Lighthill showed that the optimal flagellar shape has constant angle between the local tangent to the flagellum and the swimming direction [9]. In 2D, the sawtooth profile with a tangent angle $\varphi \approx \pm 40^\circ$ (bending angle $\beta \approx 80^\circ$) was found to optimize the swimming efficiency of an infinite length swimming filament. Alternatively, this solution can be obtained through a variational approach [32]. In 3D, Lighthill's solution leads to an optimal shape of a rotating helix. More recently, Spagnolie and Lauga studied the optimal shapes for both finite and infinite elastic flagellum by incorporating physical constraints such as bending and sliding costs [32]. Inspired by the investigations of optimal strategies for Newtonian swimming, we study the optimal shape for infinite swimmers in granular substrates using resistive force theory.

For bodies of infinite length, the optimal shape is time, scale and phase invariant [32]. Therefore, we take $\Lambda = L = 1$ and consider the optimization for $t = 0$. In other words, the local tangent angle for the optimization problem would be

$$\varphi(s, t = 0) = \sum_{n=1}^{n^*} a_n \cos(2\pi n s). \tag{2.27}$$

We consider the optimal filament shape by maximizing the swimming efficiency η defined in Sec. 2.2.3. Once the local tangent angle is obtained, the shape itself can be recovered by integration. The numerical methods used in this optimization can be found in Appendix A.1.

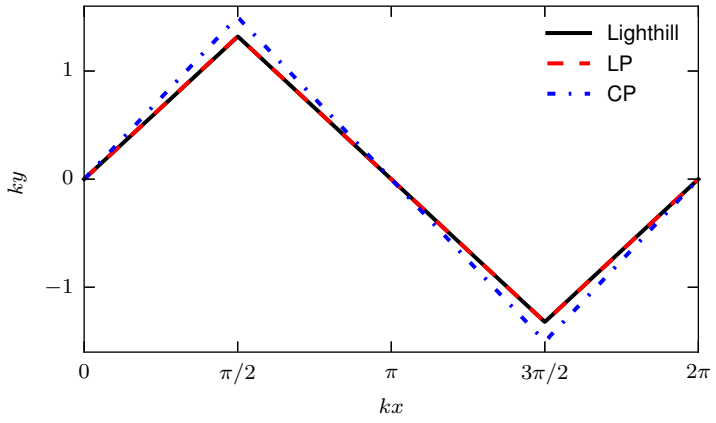

Figure 2.3: Optimal shapes in terms of swimming efficiency for an infinite filament in a granular substrate (LP, CP) and Newtonian fluid. The spatial coordinates are scaled to the same wave length. For loosely packed granular material, the optimal shape is almost the same as the analytical result of Lighthill's in Newtonian fluid.

The optimal shapes found by maximizing the swimming efficiency are presented in Fig. 2.3 for a LP granular substrate (red dashed line), a CP granular substrate (blue dash-dot line), and

a viscous Newtonian fluid (black solid line) as a comparison. First, it is interesting that the optimal shape stays as sawtooth despite the nonlinearity in the resistive force model of granular substrates. The optimal bending angles for LP and CP granular media are, respectively, $\beta \approx 80°$ and $\beta \approx 87°$. The associated efficiencies of the optimal shapes are around 0.56 for LP and 0.51 for CP granular substrates, which are much greater than that of Newtonian swimming. In spite of the difference in the surrounding media, the optimal bending angle for granular substrates and viscous Newtonian fluids lie within the same range; in particular, the optimal sawtooth in LP closely resembles that in Newtonian fluids.

We argue that it is not surprising that the sawtooth waveform is optimal in both the viscous RFT and the nonlinear granular RFT. Given an angle that maximizes the efficiency of a local element. Without any penalty, the globally optimal shape would be the one that is locally optimal everywhere along the body. As a result, a local resistive force model should exhibit an optimal shape of a certain sawtooth waveform. Using this argument, we can simply drop the integration (or assume it is a sawtooth) in Eq. (2.26) and consider the local optimality. The local optimal angle obtained is indeed the same as that found using numerical global optimization (see Sec. 2.3.2).

The existence of a locally optimal tangent angle φ originates from the physical picture introduced by the drag-based propulsion model [3] (Fig. 2.1). Let $\mathbf{u}_d = u_d \mathbf{e}_y$ be the transverse deformation velocity of an infinite swimming filament. Then a propulsive force, which is perpendicular to the direction of the deformation velocity, generated by this deformation can be given by

$$\mathbf{f}_{\text{prop}} = -(C_\perp(\psi) - C_\parallel) \sin\varphi \cos\varphi \mathbf{e}_x. \tag{2.28}$$

Therefore, the propulsive force arising from a local deformation of the filament scales with its orientation as

$$\frac{\sin\varphi\cos\varphi}{\sqrt{\tan^2\gamma_0 + \cos^2\varphi}}, \tag{2.29}$$

the maximum of which is achieved when $\varphi \approx 64°$. However, as the tangent angle increases, the power consumption of the swimming filament increases. As a result, the swimmer tends to reduce the tangent angle to decrease the energy expenditure while maintaining a relatively high propulsive force. It is the interplay of these two factors that determines the optimal tangent angle.

2.3.2 Sawtooth and sinusoid

The swimming speed of an infinite sawtooth in viscous fluids can be expressed as

$$\frac{U}{V} = \frac{1-\cos\beta}{3-\cos\beta}. \tag{2.30}$$

For a sawtooth profile in granular substrates, although an explicit analytical solution cannot be extracted, an implicit algebraic equation for the swimming speed U can be obtained since the local resistive forces do not vary along the body:

$$\left(\frac{C_S \sin\beta_0}{\sin\psi} + C_F\right)\hat{\mathbf{u}}\cdot\mathbf{e}_x - \frac{C_S \sin\beta_0}{\sin\psi}(\hat{\mathbf{u}}\cdot\mathbf{t})\mathbf{t}\cdot\mathbf{e}_x = 0, \tag{2.31}$$

where $\mathbf{t}\cdot\mathbf{e}_x = \cos(\beta/2)$. We then solve Eq. (2.31) numerically (see Appendix) with the same convergence criterion as in the optimization (Sec. 2.3.1). For a sinusoidal wave in granular media, a simplification like Eq. 2.31 is not available and we therefore directly solve Eq. (2.26) with the numerical method outlined in the Appendix.

For small amplitude sawtooth waveforms ($\epsilon \ll 1$), or small bending angle β, we obtain an asymptotic solution of the swimming speed U. Note that the swimming speed is invariant under a phase shift of π, which is equivalent to a sign change in the amplitude: $\epsilon \to -\epsilon$. Assuming a regular expansion in ϵ, this symmetry argument leads to a quadratic scaling of the swimming speed in the wave amplitude[4]

$$\frac{U}{V} \sim \frac{4\cos\gamma_0 C_S}{\pi^2 C_F}\epsilon^2. \tag{2.32}$$

When the bending angle is large, another asymptotic limit can be obtained. The swimming speed U/V approaches a constant as $\beta \to \pi$ and analytically we find that

$$\frac{U}{V} \sim \frac{C_S}{C_S + C_F\tan\gamma_0}. \tag{2.33}$$

One can also show that this large amplitude asymptotic limit for a sawtooth equals that of a sinusoidal wave. For small amplitude sinusoidal waveforms, however, the nonlinearity of the shape and the resistive forces results in a non-uniform integral and a slowly converging asymptotic series. To leading order, the swimming speed U/V scales as $\epsilon^2/\ln(1/|\epsilon|)$, which does not agree well with the numerical results even for $\epsilon < 0.1$ as the higher order terms being truncated are not significantly smaller. We present the small and large amplitude asymptotic solutions for the granular swimming of a sawtooth profile in Fig. 2.4(a). The asymptotic solutions agree well with the numerical solutions even for wave amplitudes close to one. Fig. 2.4(b) shows the efficiency of swimming as a function of the bending angle for an infinite sawtooth in both granular media and viscous fluids. For swimming efficiency, a global maximum in bending angle exists for both viscous and granular swimming. Note that the optimal angles obtained here are equal to those obtained via the global optimization (Sec. 2.3.1).

In Fig. 2.5, we compare the swimming speed and efficiency of sawtooth and sinusoidal waveforms in both GM and Newtonian fluids as a function of the wave amplitude ϵ. In both GM and Newtonian fluids, the swimming speed of a sawtooth is only slightly different from that of a sinusoid with the same dimensionless amplitude. This small difference indicates that the effects of the local curvature variations are not significant in both the granular and viscous RFT.

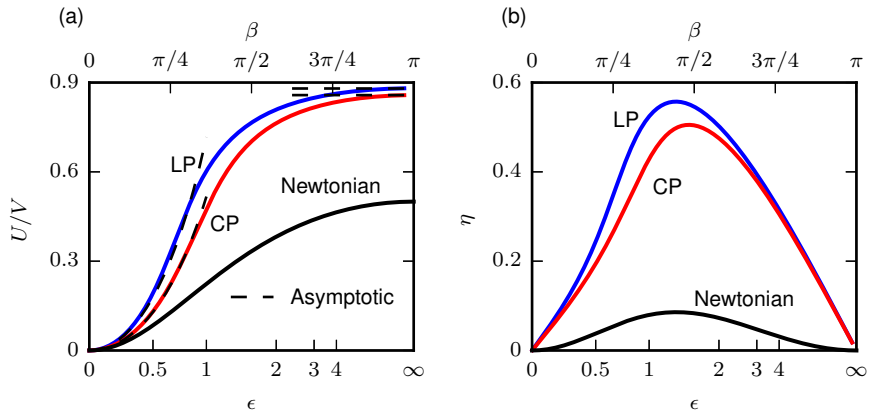

Figure 2.4: (a): Swimming speed of infinite sawtooth waveforms as a function of amplitude ϵ (or bending angle β) in granular material and Newtonian fluids. The dashed lines indicate the small and large amplitude asymptotic solutions. (b): Efficiency of infinite sawtooth waveforms as a function of amplitude ϵ (or bending angle β) in granular material and Newtonian fluids.

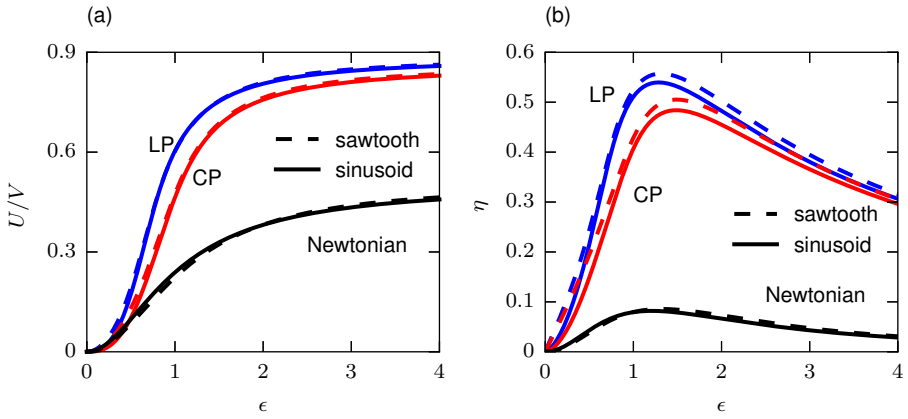

Figure 2.5: A comparison of the swimming speed (a) and efficiency (b), as a function of wave amplitude ϵ for sawtooth and sinusoidal waveforms in granular substrates and Newtonian fluids.

Although the sawtooth is found to be the mathematically optimal shape, the undulatory gait of a sandfish resembles a smooth sinusoidal waveform [20]. The slight difference in swimming performance between the two waveforms presented in this section might justify the adoption of a sinusoidal waveform instead of the mathematically optimal sawtooth waveform, since the kinks in the sawtooth may involve other energetic costs associated with bending and the deformation of the internal structure of the body [32].

2.4 Bodies of finite length

The infinite swimmer model only enforces a force balance in one direction and hence a swimmer is confined to swim only unidirectionally without any rotation. In reality, however, a swimmer has a finite size and more complex swimming kinematics, including transverse motion relative to the wave propagation direction and rotation. Previous studies employed slender body theory to investigate the swimming motion of finite filaments in a viscous Newtonian fluid and their swimming performance in relation to number of wavelengths and filament length [14, 32, 39, 40]. In this section, we investigate the swimming characteristics of finite-length sinusoidal swimmers in a granular medium and compare with their Newtonian counterparts. The numerical methods implemented to solve the equations of motion of a finite length swimmer are given in Appendix A.2.

2.4.1 Geometries

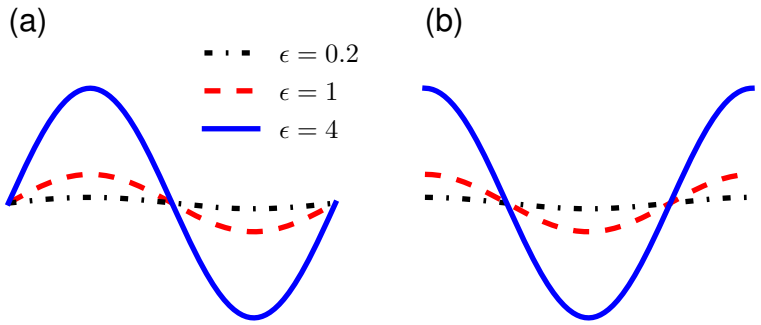

Figure 2.6: Shapes of swimming finite length single wave ($N = 1$) sinusoidal filaments for different wave amplitude ϵ. (a): the odd sine configuration, with $kX_0 = 0$, (b): the even cosine configuration, with $kX_0 = \pi/2$. The waveforms are rescaled to the same wave length for better comparison.

For an undulating sinusoidal filament, the initial shape of the swimmer is determined by the number of waves N, the wave amplitude ϵ, and the initial phase angle kX_0 (Eq. (2.23)). The two specific categories of shapes that possess odd or even symmetry for a single wave sinusoidal swimmer are shown in Fig. 2.6. A swimmer in an odd configuration is the one that has point symmetry about the midpoint of the filament as seen in Fig. 2.6(a), while an even configuration is the one that possesses mirror symmetry about the vertical line through the midpoint as in Fig. 2.6(b). In our paper, the shapes shown in Fig. 2.6(a) are referred to as odd sine swimmers, while even cosine swimmers are those shown in Fig. 2.6(b). Note that an even sine swimmer would be the one that has the number of waves $N \in \{1/2, 3/2, 5/2, ...\}$ and a phase angle $kX_0 \in \{0, \pm\pi, \pm 2\pi, ...\}$; an even cosine swimmer is the one that has the number of waves $N \in \{1, 2, 3, ...\}$ and a phase angle $kX_0 \in \{\pm\pi/2, \pm 3\pi/2, ...\}$.

2.4.2 Pitching, drifting and reorientation

Unlike the swimming of an infinite length undulatory swimmer whose motion is steady and unidirectional, the locomotion of a finite filament may also experience net motion normal to the initial direction wave propagation direction, also referred to as drifting, and unsteady rotational motion, known as pitching. Here we characterize in GM the re-orientation of a finite swimmer that results in drifting, and the dependence of swimming performance on pitching motion, previously reported to diminish performance in viscous Newtonian media [32, 40].

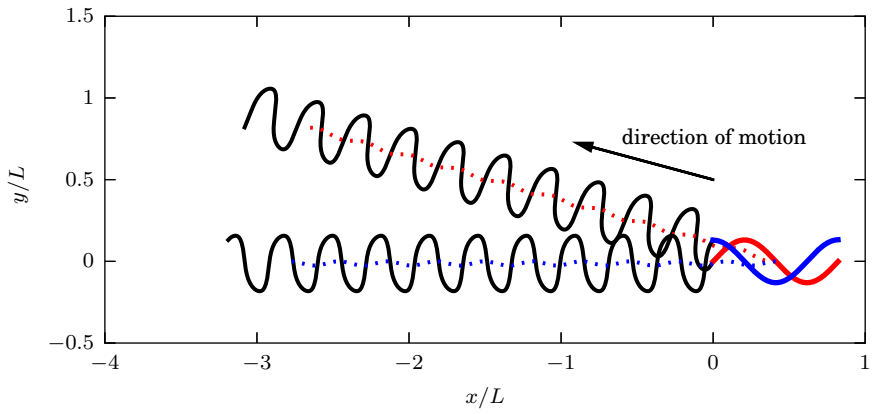

Figure 2.7: Trajectory of the head $\mathbf{x}(0,t)$ (black solid lines) and trajectory of the swimmer centroid (dotted lines) for swimming finite sinusoidal filaments with $N = 1$ and $\epsilon = 1$ that possess odd/even symmetry at $t = 0$ in loosely packed GM. The filament swims towards the left when the wave propagates to the right. If the configuration possesses even symmetry it does not undergo a net reorientation.

For an even symmetry filament in viscous fluids, Koehler *et al.* [40] showed that the velocity of the center of mass is along the centerline of the waveform, hence the net drifting is zero. This argument relies on the kinematic reversibility of Stokes flow: reflection about the vertical line is equivalent to a time reversal (or reversing the direction of the actuation), so the instantaneous swimming is identical to the mirror reflection of its time-reversal, and the linearity requires the reverse of velocity due to time-reversal, thus one can show that the transverse component of the velocity is zero. As a result, the net displacement in one period for a filament starts with the even configuration is along the initial waveform centerline.

Although the granular RFT is nonlinear, the aforementioned symmetry property ($\mathbf{u} \to -\mathbf{u} \Rightarrow \mathbf{f} \to -\mathbf{f}$, see Sec. 2.2.2) means that the same argument for an even symmetry swimmer can be made in GM. Therefore, zero net transverse motion is achieved if the swimmer starts with an even symmetry, which is also corroborated by the numerical simulation. Fig. 2.7 shows the head trajectories of two swimming sinusoidal filaments with the same wave amplitude ($\epsilon = 1$), one starts with even symmetry while the other starts with odd symmetry. The net displacement of the even cosine swimmer is in the negative x-direction, which is the opposite direction of the wave propagation at $t = 0$. The odd sine swimmer, however, appears to be drifting upwards to

the positive y-direction through time.

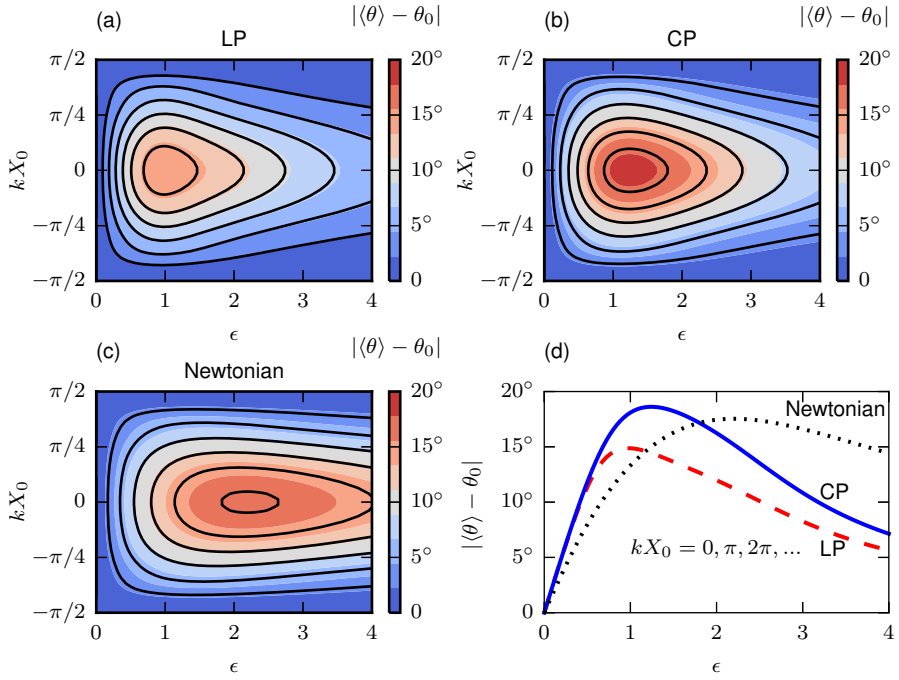

Figure 2.8: Parametric plots for the magnitude of the reorientation angle $|\langle\theta\rangle - \theta_0|$ for a single wave ($N = 1$) sinusoid in (a) loosely packed GM, (b) closely packed GM and (c) Newtonian fluids. (d): Plots of $|\langle\theta\rangle - \theta_0|$ against the wave amplitude ϵ for the odd sine configuration in GM and Newtonian fluids. $|\langle\theta\rangle - \theta_0|$ is periodic with a period of π.

The swimming behavior presented in Fig. 2.7 can be understood by examining the periodic instantaneous motion of the swimmer. In the moving frame, or the Lagrangian frame, the instantaneous motion of the swimmer can be viewed as being pulled through a waveform-shaped tube [40]. This motion, in turn, causes rotation and translation of the Lagrangian frame. The instantaneous rotation of the Lagrangian frame is described by $\theta(t)$, which is periodic due to the periodicity of the wave propagation. The average of $\theta(t)$ over one period, denoted as $\langle\theta\rangle$, describes the average swimming direction. This angle $\langle\theta\rangle$ is the same in every period which results in a straight line trajectory on average. If a filament, starts with an odd (even) configuration at $t = 0$ (if aligned with the x-axis then $\theta_0 = 0$), it would possess even (odd) symmetry at $t = T/4$. Thus the filament alternates between even symmetry and odd symmetry after successive time steps of $T/4$. In this viewpoint, $\langle\theta\rangle - \theta_0$ characterizes the amount of time t_1 required for the filament to reorient itself such that it reaches an even symmetry. After that, the swimmer would move in the direction of the waveform centerline at $t = t_1$. For a fixed number of waves N and amplitude ϵ, the odd configuration requires the largest amount of time ($T/4$) to reach an even symmetry, therefore has the largest angle of reorientation. Note that the angle of reorientation should be distinguished from pitching of the swimmer, which is the instantaneous rotation of the swimmer about its waveform centerline.

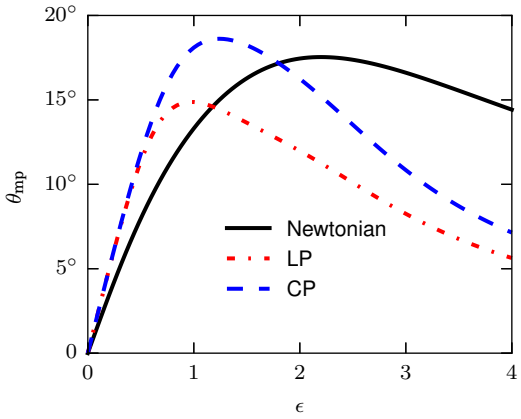

Figure 2.9: Maximum instantaneous pitching angle θ_{mp} as a function of the wave amplitude ϵ for single wave ($N = 1$) sinusoidal swimmers in GM and Newtonian fluids.

In Fig. 2.8, we present parametric plots of absolute value of the angle of reorientation $|\langle\theta\rangle - \theta_0|$ by varying the wave phase angle kX_0 and the amplitude ϵ in both GM and viscous fluids. The number of waves is fixed as $N = 1$, which approximates the shape of an undulating sandfish body [20]. Note that a phase shift of π would result in a reversal of the direction of the transverse motion, hence the sign of $\langle\theta\rangle - \theta_0$. In both GM and Newtonian fluids, the maximum in $|\langle\theta\rangle - \theta_0|$ is obtained when the filament possesses an odd symmetry at $t = 0$, i.e., $kX_0 \in \{0, \pi, 2\pi, ...\}$. For shapes that possess even symmetry, namely, $kX_0 \in \{\pi/2, 3\pi/2, ...\}$, zero transverse motion is observed. Within our parameter range, a maximum in $|\langle\theta\rangle - \theta_0|$ is achieved around an intermediate value of the amplitude for a given phase angle. As an example, the variation of $|\langle\theta\rangle - \theta_0|$ with the amplitude ϵ for the odd configuration is shown in Fig. 2.8(d). The largest amount of reorientation of an odd swimmer is achieved when $\epsilon \approx 1 - 1.2$ in GM while $\epsilon \approx 2.2$ in viscous fluids. We also note that the angle of reorientation decreases with the increasing of wave amplitude in the large amplitude region ($\epsilon > 2$).

Although the transverse motion of the even configuration is minimal, the instantaneous pitching, $\theta(t) - \langle\theta\rangle$, which generally diminishes performance, can be significant. Multiple metrics have been used to characterize pitching of a swimmer [32, 40], here we use the maximal amount of instantaneous pitching a swimmer can experience in one cycle of its motion $\theta_{mp} = |\theta(t) - \langle\theta\rangle|_{max}$. Fig. 2.9 shows the maximal instantaneous pitching angle θ_{mp} for single wave sinusoidal swimmers in GM and Newtonian fluids. The maximal instantaneous pitching angle of a single wave sinusoid goes up to about 15° in loosely packed GM while around 19° in closely packed GM.

The instantaneous pitching of the swimmer results in a tortuous motion with a net swimming speed smaller than that of an infinite sinusoid. For a fixed number of waves and wave amplitude, a phase shift only leads to a variation in the direction of swimming. In other words, the velocity magnitude U is independent of kX_0 but the x and y components vary. From a control point of

view, one can change the phase angle of an artificial sinusoidal swimmer to obtain the desired direction of swimming.

2.4.3 Swimming performance

The two typical metrics for swimming performance used in the literature are the dimensionless swimming speed U/V and the swimming efficiency η, see Eq. (2.21). For a sinusoidal swimmer, the performance depends on the dimensionless amplitude ϵ and the number of waves N. Note that the initial phase angle kX_0 does not affect the two performance metrics. The desired motion of a finite swimmer is its translation, therefore the optimization of a finite sinusoidal filament requires minimizing pitching.

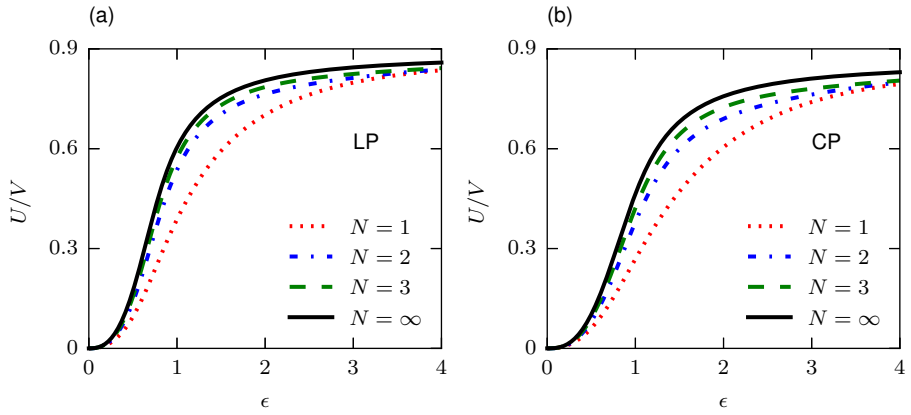

Figure 2.10: Swimming speed U/V as a function of the dimensionless amplitude ϵ for different number of waves N in (a) loosely packed GM and (b) closely packed GM. The solid lines denote the swimming speed of an infinite sinusoid.

For an undulatory finite filament in viscous fluids, several studies have characterized the swimming performance and optimal strategies. Spagnolie and Lauga reported that the local maxima in swimming efficiency occur for around half-integer number of waves ($N \approx 3/2, 5/2, ...,$) when the bending cost is small [32]. Later studies by Koehler *et al.* [40] and Berman *et al.* [41] also showed that, for a sinusoidal swimmer, local maxima in performance are achieved for close to half-integer number of waves where pitching is small.

We first verify that the swimming velocity (Fig. 2.10) and efficiency (Fig. 2.11) of a finite sinusoidal swimmer in GM both converge to that of an infinite sinusoidal swimmer as the number of waves N increases. For a single wave sinusoid ($N = 1$) in loosely packed GM, the optimal dimensionless amplitude that maximizes the efficiency is $\epsilon \approx 1.68$. As the number of waves increases, the optimal dimensionless amplitude approaches that of an infinite sinusoid ($\epsilon \approx 1.33$). Similar observations can be made for closely packed GM. We also observe that for a given dimensionless amplitude ϵ, the difference in the swimming velocity (or efficiency) between a short swimmer ($N = 1$) and an infinite swimmer can be associated with the pitching motion:

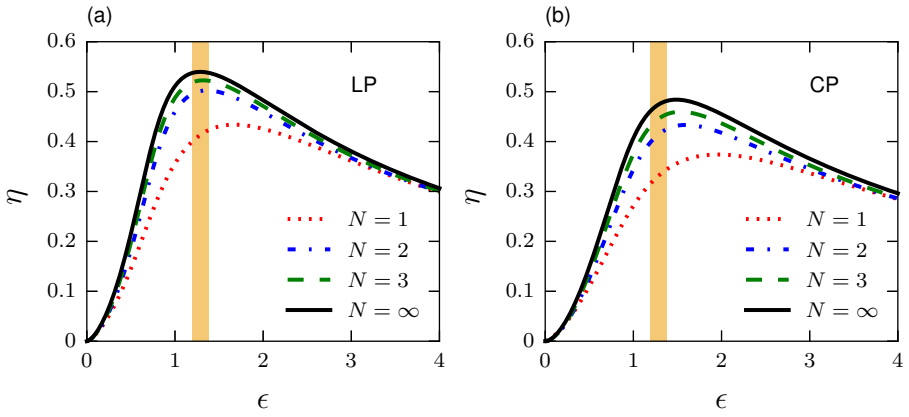

Figure 2.11: Swimming efficiency η as a function of the dimensionless amplitude ϵ for different number of waves N in (a) loosely packed GM and (b) closely packed GM. The shaded regions represent the observed values of ϵ for lizards reported in the literature [20, 21].

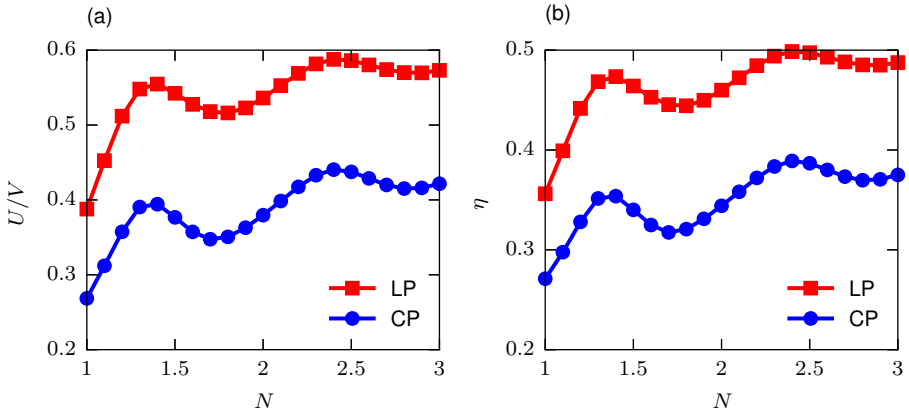

Figure 2.12: (a) Swimming speed as a function of the number of waves in GM. (b) Swimming efficiency as a function of the number of waves in GM. The dimensionless amplitude is fixed ($\epsilon = 1$).

the largest difference in swimming speed (or efficiency) between the $N = 1$ and $N = \infty$ swimmers occurs in the region $\epsilon \approx 1$ in Figs. 2.10 and 2.11, which is also the region where pitching is the most significant (Fig. 2.9).

For a given waveform, the amount of pitching can be altered by changing the number of waves N. We investigate in Fig. 2.12 the dependence of the performance metrics on the number of waves for a finite sinusoidal swimmer, keeping dimensionless amplitude fixed at $\epsilon = 1$. Rather than approaching the swimming velocity (or efficiency) of the corresponding infinite sinusoid monotonically with increasing number of waves, the swimming speed and efficiency exhibit local maxima and minima. Similar to the Newtonian case, the local maxima in efficiency and swimming speed occur for the number of waves close to (but not equal) half-integers. The

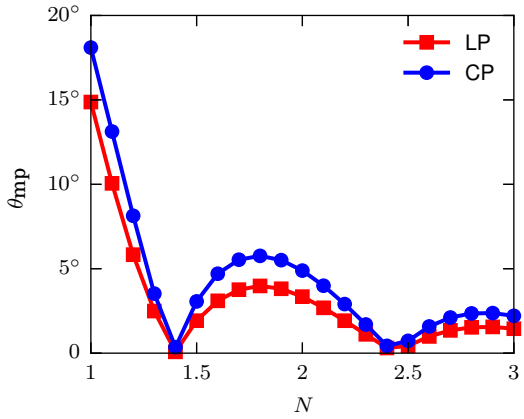

Figure 2.13: Maximum instantaneous pitching angle as a function of the number of waves in GM. The dimensionless amplitude is fixed ($\epsilon = 1$).

volume fraction of the GM has no significant influence on the number of waves where local maxima in swimming performance occur. As shown in Fig. 2.12, the first local maximum in swimming performance for the number of waves greater than one occurs around $N \approx 1.4$. The maxima in swimming performance are associated with minimal pitching as shown in Fig. 2.13. Finally we note that although both the first two local maxima have minimal pitching (Fig. 2.13), the swimmer with more number of waves ($N \approx 2.5$) still displays better swimming performance, which can be attributed to a smaller bobbing motion [40] (the relative motion of the center of mass of the swimmer to the net swimming direction) for the swimmer with more number of waves.

Finally, we relate our findings to biological observation; we show, in the shaded regions of Fig. 2.11, the observed dimensionless amplitude (amplitude-to-wavelength ratio) for lizards reported in the literature ($\epsilon = 1.20-1.38$) [20, 21]. We see in the case of both loosely-packed and closely-packed granular media, that the biologically observed range of wave amplitudes sample high efficiencies not far from optimal ($\epsilon \approx 1.69$ for LP and $\epsilon \approx 1.95$ for CP for $N = 1$). Since the efficiency peak is broad, a swimmer may adopt a close-to-optimal shape at the expense of only a modest drop in swimming efficiency to address other constraints (such as bending costs or internal dissipation).

2.5 Conclusion

In this chapter, we have investigated locomotion of slender filaments in granular media using a resistive force theory proposed by Maladen *et al.* [20]. While previous work focused on infinite swimmers (or 1-D swimming) in reality a swimmer has a finite size, which leads to more complex swimming motion. By taking into account full force and torque balances, a finite swimmer is no longer only confined to swim in a straight trajectory. The orientation of the swimmer can be

controlled by adjusting the features of the waveform such as the amplitude, phase, and number of wavelengths, allowing a swimmer to move from an initial position to a final destination via a more complex, designated trajectory. These degrees of freedom enable the control of swimmers without the use of any external fields to actively steer the swimmer. Our studies characterize this complex swimming motion in granular media, which may be useful for the development of programmable and efficient autonomous locomotive systems in such environments, but also suggest that swimmers in nature are themselves closely tuned for optimality.

We also find that undulatory locomotion of filaments in granular media is distinctly similar to that in viscous fluids. We compared a number of observations made for swimming in viscous fluids with RFT both for finite and infinite swimmers and found qualitatively similar behavior using granular resistive force theory despite the nonlinearity of the force law. The reason is largely down to two distinct similarities. The first, is that both laws are still local and thus ignore interactions of distinct parts of the body through the medium in which they swim. Ultimately this leads to finding that a sawtooth profile optimizes locomotion in both viscous fluids and granular media. The second, is that both force laws display the symmetry that $\mathbf{u} \to -\mathbf{u}$ results in $\mathbf{f} \to -\mathbf{f}$. This leads to a kinematic reversibility in both cases, where a reversal of the wave speed leads to a reversal of the translational and rotational motion of the swimmer, and hence a myriad of qualitatively similar behaviors that we have explored and quantified in this chapter.

Chapter 3

Optimal flexibility of a driven microfilament in a viscous fluid

3.1 Introduction

In many situations of biological locomotion in fluids, such as flapping birds, swimming fish and beating flagella, propulsive thrust is achieved by periodic motion of a flexible body or appendage [3, 36, 42]. Elastic deformations of flexible parts on a swimmer due to the fluid-structure interaction can lead to significantly improved propulsive performance across Reynolds numbers [4, 43, 44]. However, the physics of swimming at small scales relevant to microorganisms are fundamentally different from that of the mesoscopic swimming of flexible bodies.

For swimming microorganisms such as flagella and bacteria, the dominance of viscous forces over inertial effects leads to the time-reversible Stokes equations governing the fluid motion. In this low Reynolds number regime, Purcell's famous "scallop theorem" states that a reciprocal motion (a deformation that exhibits time-reversal symmetry) cannot generate any net propulsive thrust [5]. In order to break the constraint of time-reversibility, many microorganisms including flagellated bacteria and spermatozoa achieve self-propulsion by passing deformation waves along their flexible bodies [3, 6, 7]. Advances in fabrication technologies at small scales allow the recent rapid development of synthetic micro-propellers capable of swimming at speeds comparable with microorganisms. In particular, slender flexible filaments have been employed to enable locomotion at small scales [45–48].

A rigid filament driven at one end cannot propel itself because the motion is reciprocal. By introducing flexibility in the filament, the coupling between the viscous and elastic forces produces deformation along the filament that can lead to propulsion [49, 50]. For a given actuation frequency and filament length, an optimal bending stiffness of the filament can be determined to produce the largest propulsive force [4, 49, 51]. However, the possibility of further improving the propulsion by allowing variable flexibility along the filament remains largely unexplored. Flying animals such as hoverflies and hummingbirds exhibit non-uniform flexibility distribution along their wings, which can potentially enhance the propulsive performance [52, 53]. For a flapping wing in this high Reynolds number regime, Shoele and Zhu [54] have compared the performance of several cases of nonuniform flexibility distributions and a recent work by Moore [55] has shown that optimal propulsion can be achieved by a highly localized flexibility arrange-

ment at the front of the wing using a torsional spring. At low Reynolds numbers, Maier *et. al.* [48] have constructed a flagellar bundle attached to a magnetic head using DNA tile-tube assembly where they achieved an exponentially decreasing stiffness profile. They found that for several starting stiffnesses at the basal end, the swimmer with an exponentially decreasing stiffness profile outperforms the one that has uniform stiffness down along the flagellum under a rotational actuation using an external magnetic field. However, they did not attempt a systematic parameter study or an optimization.

In this work, we consider the propulsive force generated by a boundary displacement-driven passive cantilever filament at low Reynolds number. The mathematical formulation allows variable bending flexibility, and we derive analytically the expressions for the propulsive force of a filament with two segments of different bending flexibilities connected serially together, a torsional spring connected to a rigid rod and an arbitrarily continuous distribution of bending flexibility using asymptotic analysis for small actuation amplitude. We show that, different from the high Reynolds number case, the torsional spring arrangement does not optimize the propulsion. From a numerical optimization, we show the optimal linear and quadratic distribution of flexibility. By considering two other different boundary conditions, we show that the optimal flexibility arrangement can be qualitatively modified so that one can not simply extend the optimality for one case to other cases where the boundary actuation mechanisms differ.

This Chapter is organized as follows. We formulate the problem and review the classical results of a boundary-driven passive filament with uniform bending stiffness in Sec. 3.2. A filament with two segments that have different bending stiffnesses is first considered (Sec. 3.3): we show that this arrangement can achieve a higher propulsive thrust than the maximum of a uniform case. In Sec. 3.4, we calculate the propulsion generated by a torsional spring arrangement. Then we consider a numerical optimization over several cases of continuous stiffness distribution in Sec. 3.5. Next, we discuss the effect of boundary conditions by considering two different mechanisms of actuation in Sec. 3.6, before concluding the work with remarks in Sec. 3.7.

3.2 Mathematical formulation

We consider a slender cylindrical filament of length L and uniform radius a such that $a \ll L$ and assume the filament is elastic and inextensible. The deformation of the filament is assumed to be confined in the x-y plane. We define the position vector of a material point on the filament neutral line relative to the laboratory frame as $\mathbf{x}(s,t)$, where s is the arclength along the filament with $s \in [0, L]$ at time t. It is convenient to describe the shape of the filament by the local tangent angle made with the x-axis as $\psi(s,t)$ such that

$$\mathbf{x}_s = [\cos\psi, \sin\psi]^{\mathsf{T}}, \tag{3.1}$$

where the subscript s denotes differentiation with respect to s, namely $\mathbf{x}_s \equiv \partial_s \mathbf{x}$. The local unit tangent and normal vectors at location s along the filament are defined as $\mathbf{t}$ and $\mathbf{n}$ respectively,

with $\mathbf{t} = \mathbf{x}_s$. The local geometry is thus characterized by the Frenet-Serret formulas:

$$\mathbf{t}_s = \mathbf{x}_{ss} = \kappa \mathbf{n}, \quad \mathbf{n}_s = -\kappa \mathbf{t}, \tag{3.2}$$

where $\kappa = \|\mathbf{x}_{ss}\| = \psi_s$ is the local curvature.

3.2.1 Enthalpy functional

In order to model the dynamics of the driven filament, we start from an enthalpy functional

$$\mathcal{E} = \frac{1}{2}\int_0^L A\mathbf{x}_{ss}^2 \,\mathrm{d}s + \frac{1}{2}\int_0^L \sigma\left(\mathbf{x}_s^2 - 1\right)\mathrm{d}s, \tag{3.3}$$

where $A = A(s) = EI$ is the bending stiffness which we allow to vary along the filament with E the Young's modulus and I the second moment of inertia of the cross-section. The local inextensibility condition $\mathbf{x}_s \cdot \mathbf{x}_s = 1$ is enforced by introducing the Lagrange multiplier $\sigma(s,t)$. The internal elastic force density is determined by a variation $\delta\mathcal{E}$ with respect to a variation $\delta\mathbf{x}$ of the shape $\mathbf{x}$. Noting that

$$\delta\kappa = \delta\|\mathbf{x}_{ss}\| = \delta\left(\sqrt{\mathbf{x}_{ss}^2}\right) = \mathbf{n}\cdot\delta\mathbf{x}_{ss}, \tag{3.4}$$

we have

$$\delta\mathcal{E} = \int_0^L \left(A\kappa\mathbf{n}\cdot\delta\mathbf{x}_{ss} + \sigma\mathbf{x}_s\cdot\delta\mathbf{x}_s\right)\mathrm{d}s. \tag{3.5}$$

Upon integration by parts, we obtain

$$\begin{aligned}\delta\mathcal{E} =& \Big[A\kappa\mathbf{n}\cdot\delta\mathbf{x}_s\Big]_{s=0}^{s=L} - \Big[\partial_s\left(A\kappa\mathbf{n}\right)\cdot\delta\mathbf{x}\Big]_{s=0}^{s=L} + \Big[\sigma\mathbf{x}_s\cdot\delta\mathbf{x}\Big]_{s=0}^{s=L} \\ &+ \int_0^L \partial_s\left[\partial_s(A\kappa)\mathbf{n} - (A\kappa^2+\sigma)\mathbf{t}\right]\cdot\delta\mathbf{x}\,\mathrm{d}s.\end{aligned} \tag{3.6}$$

So the internal elastic force density is given by

$$\mathbf{f}_{\text{elastic}} = -\frac{\delta\mathcal{E}}{\delta\mathbf{x}} = -\partial_s\left[\partial_s(A\kappa)\mathbf{n} - \tau\mathbf{t}\right], \tag{3.7}$$

where we have defined $\tau = \sigma + A\kappa^2$. The boundary terms in Eq. (3.6) can be interpreted as external forces and toques applied at the two ends [56]. In other words,

$$\begin{aligned}T_{\text{ext}} &= A\kappa, \quad \mathbf{F}_{\text{ext}} = \tau\mathbf{t} - \partial_s(A\kappa)\mathbf{n} \quad \text{at} \quad s = L, \\ T_{\text{ext}} &= -A\kappa, \quad \mathbf{F}_{\text{ext}} = -\tau\mathbf{t} + \partial_s(A\kappa)\mathbf{n} \quad \text{at} \quad s = 0.\end{aligned} \tag{3.8}$$

3.2.2 Elastohydrodynamics

We describe the hydrodynamics of the viscous fluid by the resistive force theory, which is a leading-order approximation in the small filament aspect ratio a/L. The theory states that the viscous force per unit length on the filament is given by

$$\mathbf{f}_{\text{vis}} = -\left(\xi_\perp \mathbf{nn} + \xi_\parallel \mathbf{tt}\right) \cdot \mathbf{x}_t, \tag{3.9}$$

where the subscript t denotes differentiation with respect to time and $\xi_\perp$ and $\xi_\parallel$ are the normal and tangential resistive coefficients respectively. The local balance between the viscous and elastic forces

$$\mathbf{f}_{\text{vis}} + \mathbf{f}_{\text{elastic}} = \mathbf{0} \tag{3.10}$$

can be written as

$$\mathbf{x}_t = \left(\frac{1}{\xi_\perp}\mathbf{nn} + \frac{1}{\xi_\parallel}\mathbf{tt}\right) \cdot \mathbf{f}_{\text{elastic}}. \tag{3.11}$$

From the variational formulation in Sec. 3.2.1 it follows that

$$\int_s^L \mathbf{f}_{\text{vis}}\,\mathrm{d}s = \int_s^L \frac{\delta \mathcal{E}}{\delta \mathbf{x}}\,\mathrm{d}s = \left[\partial_s(A\kappa)\mathbf{n} - \tau\mathbf{t}\right](s=L) - \left[\partial_s(A\kappa)\mathbf{n} - \tau\mathbf{t}\right], \tag{3.12}$$

or

$$\tau\mathbf{t} - \partial_s(A\kappa)\mathbf{n} = \int_s^L \mathbf{f}_{\text{vis}} + \mathbf{F}_{\text{ext}}(L). \tag{3.13}$$

In other words,

$$\begin{aligned} \tau &= \mathbf{t} \cdot \left(\int_s^L \mathbf{f}_{\text{vis}}\,\mathrm{d}s + \mathbf{F}_{\text{ext}}(L)\right), \\ \partial_s(A\kappa) &= -\mathbf{n} \cdot \left(\int_s^L \mathbf{f}_{\text{vis}}\,\mathrm{d}s + \mathbf{F}_{\text{ext}}(L)\right). \end{aligned} \tag{3.14}$$

Eq. (3.14) shows that τ acts as the physical tension along the filament. Following Eq. (3.11), we obtain

$$\mathbf{x}_t = \frac{1}{\xi_\perp}\mathbf{n}\left(-\partial_{ss}(A\psi_s) + \psi_s\tau\right) + \frac{1}{\xi_\parallel}\mathbf{t}\left(\psi_s\partial_s(A\psi_s) + \tau_s\right). \tag{3.15}$$

Noting that

$$\mathbf{t}_t = (-\sin\psi, \cos\psi)^{\mathsf{T}}\,\psi_t = \psi_t\mathbf{n}, \quad \mathbf{n}_s = -\psi_s\mathbf{t}, \quad \mathbf{t}_s = \mathbf{x}_{ss} = \psi_s\mathbf{n}, \tag{3.16}$$

we differentiate Eq. (3.15) with respect to the arclength and obtain

$$\begin{aligned}\psi_t \mathbf{n} =& \frac{1}{\xi_\perp}(-\psi_s \mathbf{t})\left(-\partial_{ss}(A\psi_s) + \psi_s \tau\right) + \frac{1}{\xi_\parallel}\mathbf{t}\partial_s\left(\psi_s \partial_s(A\psi_s) + \tau_s\right) \\ &+ \frac{1}{\xi_\perp}\mathbf{n}\partial_s\left(-\partial_{ss}(A\psi_s) + \psi_s\tau\right) + \frac{1}{\xi_\parallel}\psi_s \mathbf{n}\left(\psi_s\partial_s(A\psi_s) + \tau_s\right).\end{aligned} \tag{3.17}$$

Finally, the equation of motion for the tangent angle $\psi(s,t)$ reads

$$\psi_t = \frac{1}{\xi_\perp}\left(-\partial_{sss}(A\psi_s) + \partial_s(\psi_s\tau)\right) + \frac{1}{\xi_\parallel}\psi_s\left(\psi_s\partial_s(A\psi_s) + \tau_s\right). \tag{3.18}$$

Another equation obtained is a partial differential equation (PDE) for tension $\tau(s,t)$, or equivalently from the inextensibility condition $\mathbf{t}\cdot\mathbf{t}_t = 0$:

$$\tau_{ss} - \frac{\xi_\parallel}{\xi_\perp}\psi_s^2\tau = -\partial_s(\psi_s\partial_s(A\psi_s)) - \frac{\xi_\parallel}{\xi_\perp}\psi_s\partial_{ss}(A\psi_s). \tag{3.19}$$

Eqs. (3.18) and (3.19) determine the filament dynamics. Note that $(-\psi,\tau)$ satisfies Eqs. (3.18) and (3.19) if (ψ,τ) is a solution. Once the tangent angle ψ is solved, the filament shape can be recovered by integration

$$\mathbf{x}(s,t) = \mathbf{x}(0,t) + \int_0^s (\cos\psi, \sin\psi)^{\mathsf{T}}\, \mathrm{d}s', \tag{3.20}$$

where $\mathbf{x}(0,t)$ can be obtained from Eq. (3.15) by integration with respect to time evaluated at $s = 0$.

3.2.3 Boundary conditions

The filament dynamics governed by Eqs. (3.18) and (3.19) depends on the prescribed boundary conditions. In this work, we consider a boundary driven passive filament where one end is oscillated in a controlled manner while the other end is free to move in the surrounding fluid. At the free end ($s = L$), we have force-free and torque-free boundary conditions,

$$\mathbf{F}_{\text{ext}}(L) = [\tau\mathbf{t} - \partial_s(A\kappa)\mathbf{n}]_{s=L} = \mathbf{0}, \quad T_{\text{ext}}(L) = [A\kappa]_{s=L} = 0. \tag{3.21}$$

At the actuation end (s=0), we consider a harmonic oscillation with frequency ω of the transverse position of a cantilevered filament *i.e.*,

$$y(0,t) = y_0 \sin\omega t, \quad x(0,t) = 0, \quad \psi(0,t) = 0. \tag{3.22}$$

3.2.4 Non-dimensionlization

We non-dimensionalize the governing equations with respect to a length scale L, time scale ω^{-1}, velocity scale $L\omega$ and a force scale[4] A/L^2. The resistance ratio γ, sperm number Sp and the dimensionless oscillation amplitude ϵ , respectively, are defined as

$$\gamma = \frac{\xi_\perp}{\xi_\parallel}, \quad \mathrm{Sp} = L\left(\frac{\xi_\perp \omega}{A}\right)^{1/4}, \quad \epsilon = \frac{y_0}{L}. \tag{3.23}$$

The sperm number Sp compares the magnitude of viscous and elastic forces. For a given oscillation frequency ω and length of the filament L, a larger sperm number indicates a more flexible material. For a rigid filament, the sperm number $\mathrm{Sp} \to 0$. To make analytical progress, we perform asymptotic analysis in the small amplitude oscillation limit, $\epsilon \ll 1$, to determine the filament shape order by order.

3.2.5 Propulsive thrust

In our study, we are considering the effect of flexibility distribution on the propulsive performance, hence we non-dimensionalize the thrust by $L^2\xi_\perp\omega$ which is hold constant. The instantaneous propulsive thrust is defined as the total hydrodynamic drag force in the direction of swimming:

$$F_x = -\mathbf{e}_x \cdot \int_0^1 \mathbf{f}_{\mathrm{vis}}\, \mathrm{d}s \tag{3.24}$$

where $\mathbf{e}_x$ is the unit vector in the swimming direction (x-direction in our formulation). The net propulsive thrust is the time-average of the instantaneous thrust over one period of the actuation, $F_\mathrm{p} = \langle F_x \rangle$ with $\langle ... \rangle = \int_0^{2\pi} (...)\, \mathrm{d}t/2\pi$.

For small amplitude oscillation, we write the net propulsive force as a regular series expansion in ϵ,

$$F_\mathrm{p} = \epsilon^2 F_\mathrm{p}^{(2)} + \mathcal{O}(\epsilon^4). \tag{3.25}$$

For a continuous stiffness profile $A(s)$ (dimensional), we have

$$F_\mathrm{p}^{(2)} = \frac{\gamma - 1}{\gamma \mathrm{Sp}_0^4} \left\langle \int_0^1 \psi^{(1)} \partial_s^2 (A^* \partial_s \psi^{(1)})\, \mathrm{d}s \right\rangle, \tag{3.26}$$

where $\mathrm{Sp}_0 = L[\xi_\perp \omega / A(0)]^{1/4}$ is the sperm number evaluated using the stiffness at the basal end, $A^* = A(s)/A(0)$ and $\psi = \epsilon\psi^{(1)} + \mathcal{O}(\epsilon^2)$. Note that an order ϵ boundary actuation generates a propulsive force of $\mathcal{O}(\epsilon^2)$ to leading order. For $A^* \equiv 1$, the propulsive force given by Eq. (3.26) reduces to the case of a uniform stiffness profile as given by previous work [4, 57].

[4]Since the bending stiffness A can be varying along the filament, we use the value of A at a certain material point on the body.

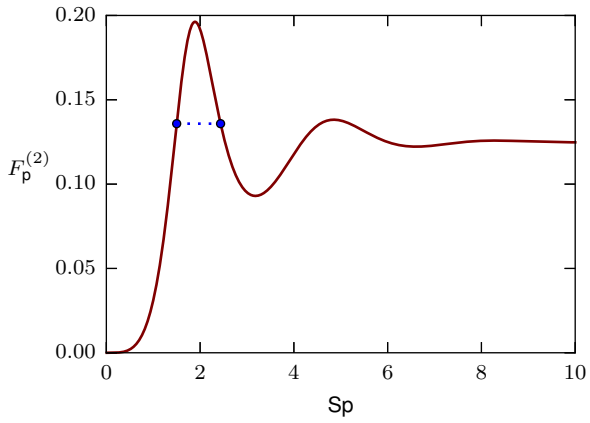

Figure 3.1: Propulsive thrust generated by a cantilevered filament of uniform bending stiffness under a displacement actuation at one extremity. The two blue dots indicate two filaments with different bending stiffnesses generating the same propulsive force.

For the classical case of uniform bending stiffness (A = constant) along the filament, the variation of propulsive force as a function of the sperm number is shown in Fig. 3.1. In the low sperm number limit (Sp $\ll$ 1), the filament becomes a rigid rod undergoing a reciprocal motion, which produces no net propulsion. For finite values of sperm number, flexibility enables the propagation of deformation waves along the body, which breaks the constraint of kinematic reversibility and generates net propulsive force. In the large sperm number limit, the dominance of viscous force over elastic force suboptimally localizes the deformation of the filament around the actuation end. Therefore, the propulsive force exhibits a maximum around an intermediate sperm number Sp $\approx$ 1.89 and asymptotes to a limiting value for large sperm numbers. The deforming shapes of a filament with uniform stiffness are shown in Fig. 3.2 for several different sperm numbers.

As indicated by the two blue dots in the proximity of the maximum propulsive force in Fig. 3.4, one can have deforming filaments of two different sperm numbers generating the same propulsive force. In other words, for a given actuation frequency and filament length one can generate the same propulsive thrust with filaments of two different bending rigidities (A_1 and A_2). Then the question is, can we still obtain the same propulsive force by serially connecting two segments that each individually generates the same propulsion, or can we enhance the propulsion?

3.3 Two-segment filaments

We probe the potential advantages of non-uniform stiffness by connecting the segments with bending flexibilities A_1 (at the actuation end) and A_2 serially as diagrammed in Fig. 3.3. The relative proportion of the segment with stiffness A_1 is denoted as α, $0 \leq \alpha \leq 1$. We define the

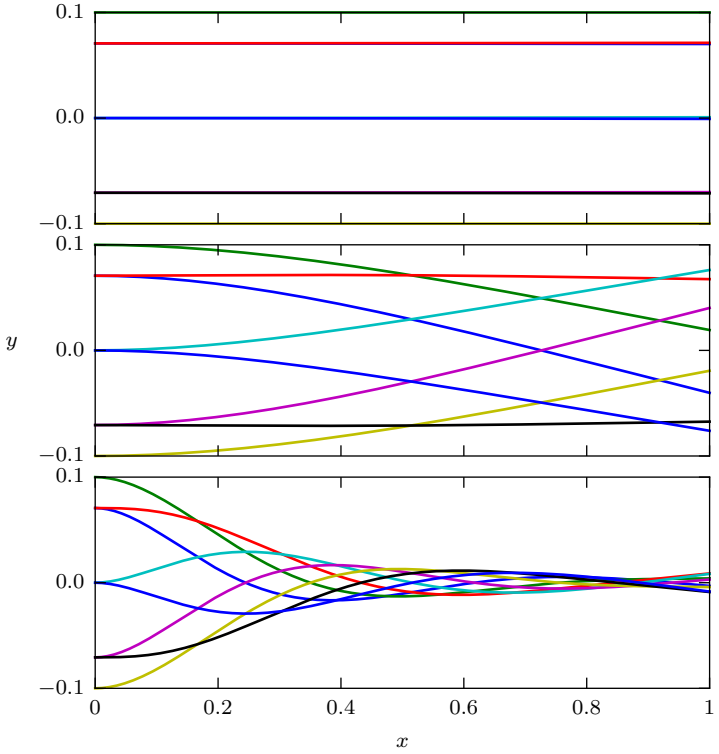

Figure 3.2: Shapes of the displace driven cantilevered filament in different times over a period. From top to bottom, the sperm number increases (top:Sp = 0.5, middle:Sp = 1.89, bottom:Sp = 8), namely, the filament becomes more flexible.

ratio of stiffness $\beta = A_2/A_1$. In this case, the local tangent $\psi(s,t)$ and tensile force $\tau(s,t)$ are split into two functions for the two segments, with ψ_k^n denoting the tangent angle of the k-th segment ($k = 1, 2$) at $\mathcal{O}(\epsilon^n)$. Noting that $\psi \sim \epsilon$, from Eqs. (3.18) and (3.19) one can show that $\tau \sim \epsilon^2$ [4]. This two-segment arrangement considered here is arguably one of the simplest cases of non-uniform flexibility distribution, and we shall show that the asymptotic analysis reveals the advantage of this simple non-uniform flexibility arrangement over the uniform case.

In the small amplitude limit, we seek a perturbative solution by using regular series expansions in ϵ,

$$\begin{aligned}
\psi_1(s,t) &= \epsilon\psi_1^{(1)} + \epsilon^2\psi_1^{(2)} + \mathcal{O}(\epsilon^3),\\
\tau_1(s,t) &= \tau_1^{(0)} + \epsilon\tau_1^{(1)} + \epsilon^2\tau_1^{(2)} + \mathcal{O}(\epsilon^3),\\
\psi_2(s,t) &= \epsilon\psi_2^{(1)} + \epsilon^2\psi_2^{(2)} + \mathcal{O}(\epsilon^3),\\
\tau_2(s,t) &= \tau_2^{(0)} + \epsilon\tau_2^{(1)} + \epsilon^2\tau_2^{(2)} + \mathcal{O}(\epsilon^3).
\end{aligned} \tag{3.27}$$

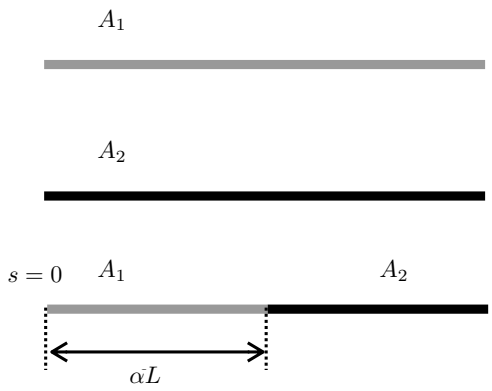

Figure 3.3: Schematic of a serially connected filament. The segment at the actuation end has a bending flexibility A_1 and the segment at the free end has a bending flexibility A_2, $\beta = A_2/A_1$.

3.3.1 Elastic-elastic case

In this section, we consider the case where both A_1 and A_2 are finite. The leading order equations of motion are written as

$$\begin{aligned} &\mathrm{Sp}_1^4 \partial_t \psi_1^{(1)} + \partial_s^4 \psi_1^{(1)} = 0, \\ &\mathrm{Sp}_1^4 \partial_t \psi_2^{(1)} + \beta \partial_s^4 \psi_2^{(1)} = 0, \end{aligned} \tag{3.28}$$

where $\mathrm{Sp}_1 = L\left(\xi_\perp \omega / A_1\right)^{1/4}$ is the sperm number of the material at the driven end.

The boundary conditions at the two ends are given by

$$\begin{aligned} \psi_1^{(1)}(0,t) = 0, \quad \partial_s^3 \psi_1^{(1)}(0,t) = -\mathrm{Sp}_1^4 \cos t \quad \text{at} \quad s = 0, \\ \partial_s \psi_2^{(1)}(1,t) = 0, \quad \partial_s^2 \psi_2^{(1)}(1,t) = 0 \quad \text{at} \quad s = 1. \end{aligned} \tag{3.29}$$

In order to solve Eq. (3.28), 4 more boundary conditions are required. Note that the tangent angle ψ should be continuous, thus we have $\psi_1^{(1)}(\alpha,t) = \psi_2^{(1)}(\alpha,t)$. Meanwhile, the internal force and moments are expected to be continuous across the connecting point, *i.e.*

$$\begin{aligned} &\partial_s \psi_1^{(1)}(\alpha,t) = \beta \partial_s \psi_2^{(1)}(\alpha,t), \\ &\partial_{ss} \psi_1^{(1)}(\alpha,t) = \beta \partial_{ss} \psi_2^{(1)}(\alpha,t). \end{aligned} \tag{3.30}$$

The last boundary condition is obtained from the continuity of the viscous force density, which states that $\partial_{sss} \psi_1^{(1)}(\alpha,t) = \beta \partial_{sss} \psi_2^{(1)}(\alpha,t)$.

Since we are interested in the steady state solution, we write the solution as

$$\begin{aligned} \psi_1^{(1)}(s,t) &= \mathrm{Re}\left\{e^{it} h_1(s)\right\}, \\ \psi_2^{(1)}(s,t) &= \mathrm{Re}\left\{e^{it} h_2(s)\right\}, \end{aligned} \tag{3.31}$$

where $i = \sqrt{-1}$ is the imaginary unit. Then Eq. (3.28) reduces to two ordinary differential equations (ODEs), which can be solved analytically.

The leading order propulsive force in this case is given by

$$F_{\mathrm{p}}^{(2)} = \frac{\gamma - 1}{2\gamma \mathrm{Sp}_1^4} \left\langle (\partial_s \psi_1^{(1)}(0,t))^2 - \left[(\partial_s \psi_1^{(1)}(\alpha,t))^2 - \beta (\partial_s \psi_2^{(1)}(\alpha,t))^2 \right] \right\rangle . \tag{3.32}$$

Note that if $\beta = 1$, $\alpha = 0$ or $\alpha = 1$, the expression for propulsive force reduces to the result for a filament with uniform stiffness.

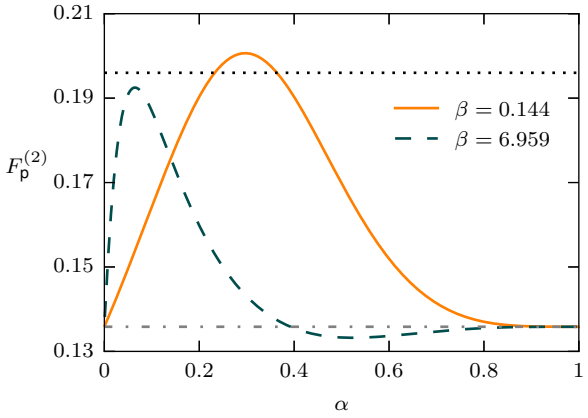

Figure 3.4: Propulsive thrust generated by two-segment filaments as a function of α at different values of stiffness ratio β. For $\beta = 0.144$ ($A_2 < A_1$, more flexible materials at the *free* end), the maximum propulsive force generated is greater than the maximum achievable thrust of a filament with any uniform stiffness.

For given sperm numbers of two materials indicated by the blue dots in Fig. 3.1, by varying the relative proportion of the two segments, a non-monotonic variation of the propulsive force emerges (Fig. 3.4). The limits $\alpha = 0, 1$ reduce to the case of uniform stiffness with a propulsive force $F_{\mathrm{p}}^{(2)} = 0.1358$ as indicated by the horizontal dash-dotted line in Fig. 3.4. The solid line denotes putting the more flexible material at the free end while the dashed line indicates putting the more flexible material at the driven end. It is interesting to note that the propulsive force generated by the two-segment filament can be greater than the original uniform case ($\alpha = 0, 1$) for both arrangements. For $\beta = 6.959$, the filament outperforms the original uniform case in the range $\alpha \lesssim 0.4$. For $\beta = 0.144$, the two-segment filament outperforms the original uniform case for almost all α.

Furthermore, by putting a more flexible material at the *free* end *i.e.* $\beta < 1$ (e.g. $\beta = 0.144, A_2 < A_1$, solid line, Fig. 3.4), the propulsive force generated by such an arrangement can be greater than the maximum possible propulsive thrust (indicated by the horizontal dotted line in Fig. 3.4) achievable by a filament with *any* uniform bending stiffness. This enhancement in propulsion indicates that the filament prefers to have a more flexible part at the free end

with an optimal choice of α.

3.3.2 Rigid-elastic case

The limiting case from the elastic-elastic arrangement would be to consider an rigid-elastic filament with $A_1 = \infty$. In other words, the segment at the driven end is rigid. For the rigid part, the local tangent angle is independent of s, *i.e.*

$$0 = \psi_1 = \psi_1(t) = \psi_2(\alpha, t). \tag{3.33}$$

As a result, one only needs to solve the PDE for ψ_2. Following similar procedure to the elastic-elastic case, we solve the governing equations to leading order. The two boundary conditions at the free end is the same as the elastic-elastic case. The boundary conditions at α are given by $\psi_2^{(1)}(\alpha, t) = 0$ and $\partial_s^3 \psi_2^{(1)}(\alpha, t) = -\mathrm{Sp}_2^4 \cos t$. Note that Sp_2 is the sperm number evaluated using the stiffness (A_2, finite) of the flexible part. The leading order propulsive force in this case reads

$$F_\mathrm{p}^{(2)} = \frac{\gamma - 1}{2\gamma \mathrm{Sp}_2^4} \left\langle (\partial_s \psi_2^{(1)}(\alpha, t))^2 \right\rangle. \tag{3.34}$$

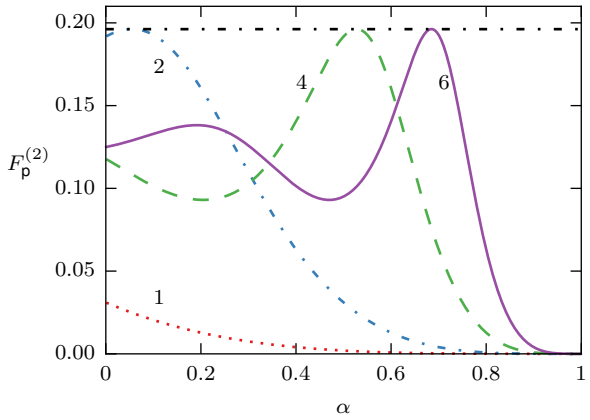

Figure 3.5: Propulsive thrust generated by a cantilevered rigid-elastic filament under displacement oscillation as a function of α for different sperm numbers Sp_2, which are indicated by the numeric values around each line. The horizontal dash-dotted line denotes the maximum propulsion of a filament with uniform stiffness.

In Fig. 3.5, we present the leading order propulsive force as a function of the proportion of the rigid part for different sperm numbers of the flexible part. For small sperm numbers, the propulsive force decreases monotonically as α increases because the rigid part does not contribute. For larger sperm numbers ($\mathrm{Sp}_2 > 2$), we observe a non-monotonic variation of propulsion as α increases from zero to one. It is interesting to note that the optimal propulsion

a rigid-elastic filament can achieve is around the maximum propulsion of a filament with uniform stiffness as indicated by the horizontal dash-dotted line in Fig. 3.5. In other words, a rigid-elastic filament cannot outperform the optimal uniform case, which means that an optimal two-segment arrangement should be an elastic-elastic one, *i.e.*, both A_1 and A_2 remain finite.

3.3.3 Elastic-rigid case

Before discussing a filament with a continuously varying stiffness profile, it is interesting to investigate an elastic-rigid filament with $A_2 = \infty$. In other words, the segment at the free end is rigid. For the rigid part, the local tangent angle is independent of s, *i.e.*

$$\psi_2 = \psi_2(t) = \psi_1(\alpha, t). \tag{3.35}$$

As a result, one only needs to solve the PDE for ψ_1. Following similar procedure to the elastic-elastic case, we solve the governing equations to leading order. The two boundary conditions at the driven end is the same as the elastic-elastic case. A force balance on the rigid part requires that

$$\partial_s^2 \psi_1^{(1)}(\alpha, t) = (\alpha - 1)\partial_s^3 \psi_1^{(1)}(\alpha, t) - \partial_s^4 \psi_1^{(1)}(\alpha, t) \left(\frac{1}{2} - \alpha + \frac{\alpha^2}{2} \right). \tag{3.36}$$

The fourth boundary condition is obtained via a torque balance on the rigid filament,

$$-\partial_s \psi_1^{(1)}(\alpha, t) + \frac{1}{2}(1-\alpha)^2 \partial_s^3 \psi_1^{(1)}(\alpha, t) + \frac{1}{3}(1-\alpha)^3 \partial_s^4 \psi_1^{(1)}(\alpha, t) = 0. \tag{3.37}$$

The leading order propulsive force is expressed as

$$\begin{aligned} F_{\mathrm{p}}^{(2)} = \frac{\gamma - 1}{\gamma \mathrm{Sp}_1^4} \Big\langle & \psi_1^{(1)}(\alpha, t) \partial_s^2 \psi_1^{(1)}(\alpha, t) - \frac{1}{2}(\partial_s \psi_1^{(1)}(\alpha, t))^2 \\ & + \frac{1}{2}(\partial_s \psi_1^{(1)}(0, t))^2 + (1-\alpha)\psi_1^{(1)}(\alpha, t)\partial_s^3 \psi_1^{(1)}(\alpha, t) \Big\rangle. \end{aligned} \tag{3.38}$$

In Fig. 3.6, we present the variation of propulsive force generated by an elastic-rigid filament as a function of α for different sperm numbers of the flexible part. We note that the optimal elastic-rigid filament cannot outperform the maximum of a uniform case. For a relatively small sperm number (e.g., $\mathrm{Sp}_1 < 2$), we observe in general a monotonic increasing of the propulsive force as the proportion of the flexible part increases from 0 to 1. When $\alpha = 0$, the filament becomes a rigid rod so that the propulsion generated is zero due to the time-reversibility of the non-deforming motion. As α increases, the proportion that can deform due to the interaction between the viscous force and elastic force increases. As a result, one can observe an increase in the propulsive performance. However, for a larger sperm number of the flexible part, a non-monotonic behavior of the propulsive force is observed as α increases. Take $\mathrm{Sp}_1 = 3$ as an example, the maximum propulsive force $F_{\mathrm{p}}^{(2)} \approx 0.1875$, which is achieved when $\alpha \approx 0.039$. As

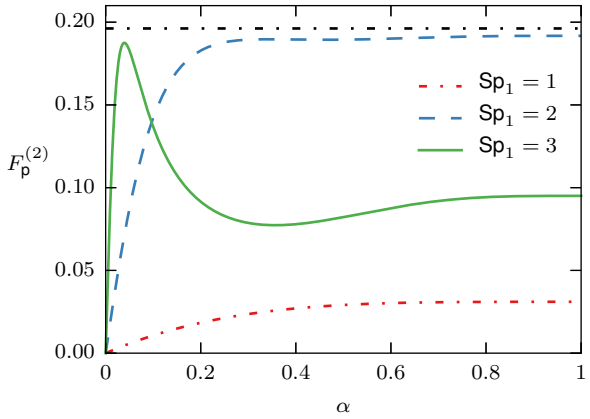

Figure 3.6: Propulsive thrust generated by an elastic-rigid filament ($A_2 = \infty$) as a function of α for different sperm numbers of the flexible part. For small sperm numbers, a monotonic increasing of the propulsive thrust is observed as α increases. For larger sperm numbers, however, the variation of propulsive thrust is non-monotonic. Note that the sperm number of the rigid part would be zero. The horizontal dash-dotted line denotes the maximum propulsive force achievable by a filament with uniform stiffness.

the sperm number Sp_1 increases, namely the flexible part becomes more flexible, the optimum propulsive force is achieved at a smaller α. For sperm numbers larger than 2, the optimal elastic-rigid arrangement exhibits a localized flexibility around the actuation end while the propulsion is predominantly generated by the rigid part at the free end. In this scenario, the tiny flexible bit at the driven end is effectively setting an optimal angle for the rigid part, which maximizes the propulsion. From fundamental beam theory, we may scale the deflection δ (dimensional) of the connecting point as

$$\delta \sim \frac{Fl^3}{A_1}, \tag{3.39}$$

where $l = \alpha L$ is the dimensional length of the flexible bit and F the effective total hydrodynamic force at this point. Noting that $F \sim L^2 \xi_\perp \omega$, and the average angle at the connecting point $\psi \sim \delta / l$, we recover the physical scaling

$$\psi \sim \frac{l^2 L^2 \xi_\perp \omega}{A_1} = \mathrm{Sp}_1^4 \alpha^2. \tag{3.40}$$

Note that $\mathrm{Sp}_1^4 \alpha^2$ is the effective sperm number of the flexible part upon a proper scaling of the elastic force, namely, we have

$$\mathrm{Sp}_{\mathrm{proper}} = \left(\frac{L^2 \xi_\perp \omega}{A_1 / l^2} \right)^{1/4}. \tag{3.41}$$

These observations presented above lead us to considering the limiting case of an entirely rigid filament with a torsional spring at the actuation end, which we shall show would be the optimal elastic-rigid arrangement upon an optimal choice of the spring constant.

3.4 Torsional spring

We consider a rigid filament of length L connected by a torsional spring with a spring constant C at the actuation end. In this scenario, the local tangent on the entire filament is independent of s, *i.e.*, $\psi(t) = \epsilon\psi^{(1)} + \mathcal{O}(\epsilon^2)$.

The torque balance of the filament reads

$$\mathbf{e}_z \cdot \int_0^1 [\mathbf{x}(s,t) - \mathbf{x}(0,t)] \times \mathbf{f}_{\text{vis}} \, \mathrm{d}s - K\psi = 0, \tag{3.42}$$

where $K = C/L^3\xi_\perp\omega$ is the dimensionless spring constant. At leading order, we have

$$\frac{1}{3}\dot{\psi}^{(1)} + \frac{1}{2}\cos t + K\psi^{(1)} = 0, \tag{3.43}$$

with $\psi^{(1)}(0) = 0$. The long time solution is given by

$$\psi^{(1)}(t) = -\frac{3}{2 + 18K^2}\left(3K\cos t + \sin t\right). \tag{3.44}$$

Finally, we obtain a simple analytical expression for the dimensionaless propulsive force $F_{\text{p}} = \epsilon^2 F_{\text{p}}^{(2)} + \mathcal{O}(\epsilon^4)$:

$$F_{\text{p}}^{(2)} = \frac{\gamma - 1}{\gamma}\frac{9K}{4(1 + 9K^2)} \tag{3.45}$$

We plot the variation of the propulsive force generated by a torsional spring arrangement as a function of the dimensionless spring constant in Fig. 3.7. As a limiting case of the two-segment filament, the torsional spring arrangement represents a highly localized flexibility focused at the actuation end with the rest of the filament being rigid, thus a straight line shape is maintained during the actuation with the tangent angle $\psi(t)$ adjusted by the torque balance. In other words, torsional spring is the optimal elastic-rigid arrangement. The leading order velocity of a local material point along the rigid filament is in the $\pm\mathbf{e}_y$ direction. If we assume a local element ds at s has a velocity $\mathbf{u} = u\mathbf{e}_y$, the resulting propulsive force density at this point scales with the geometry as $f_{\text{prop}} \sim \cos\psi \sin\psi$ [3], the extremum of which is obtained for $\psi = \pm 45°$. This physical scaling means that a filament can achieve higher propulsion by spending more time around the optimal tangent angle in one period (*i.e.*, $\langle|\psi^{(1)}|\rangle$ should be close to 45°). For the torsional spring arrangement, $\langle|\psi^{(1)}|\rangle = 9K/(\pi(1 + 9K^2))$ has a maximum of $3/(2\pi)$ ($\approx 27°$) which is obtained exactly at $K = 1/3$ where the optimal propulsion is also achieved. As K deviates from this optimal value, $\langle|\psi^{(1)}|\rangle$ decreases so that the propulsion becomes suboptimal.

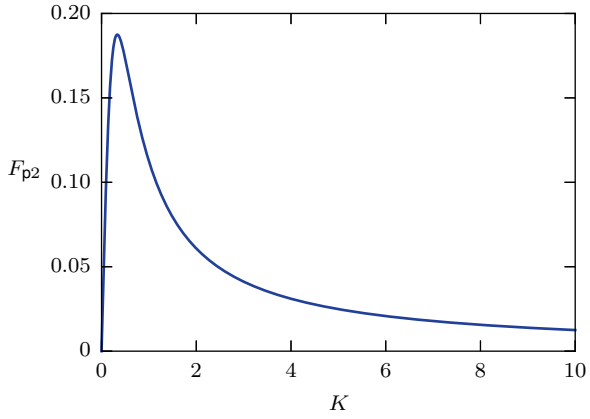

Figure 3.7: Propulsive thrust generated by a torsional spring arrangement at the actuation end connected to a rigid filament as a function of the spring constant. The optimum propulsive force is $F_{\mathrm{p}}^{(2)} = 0.1875$.

Up to this section, via a discrete approach we have shown that both elastic-rigid and rigid-elastic cannot outperform the optimal uniform case but an elastic-elastic distribution can actually enhance the propulsion as compared to the uniform filament. This begs the question: If we allow the stiffness to vary continuously along the filament, what is the optimum stiffness profile?

3.5 Continuous optimization

With the cases of two-segment and localized flexibility arrangements understood, we now allow the bending stiffness to vary continuously along the entire filament. Using Eqs. (3.18) and (3.19), the asymptotic analysis shows that at order ϵ we have

$$\mathrm{Sp}_0^4 \partial_t \psi^{(1)} + \partial_s^3 \left(A^* \partial_s \psi^{(1)} \right) = 0, \tag{3.46}$$

where Sp_0 and $A^* > 0$ are defined in Sec. 3.2. By writing $\psi^{(1)} = \mathrm{Re}\{e^{it} h(s)\}$, we solve the resulting ODE for $h(s)$ using Matlab's build-in *bvp4c* solver for a given stiffness profile A^*. As a validation of the algorithm, we solved $h(s)$ using a regularized tanh stiffness profile to approximate an elastic-elastic filament as discussed in Sec. 3.3.1, and the numerical results matched very well with the analytical solutions. Once the evolution of the filament shape is obtained, the propulsive force can be evaluated from Eq. (3.26) where Gauss-Legendre quadrature is used to calculate the numerical integration in space and time.

Now, we want to understand which continuous distribution of stiffness optimizes the propulsive performance of a driven filament. Following the procedure obtained by Moore [55] in the high Reynolds number case, we perform numerical optimization of the propulsive force over a

linear, quadratic and cubic distribution of bending stiffness, namely $A^* = as^3 + bs^2 + cs + 1$. As the degree of the polynomial distribution increases, one would expect a better approximation towards an arbitrary continuous stiffness profile. The optimization is performed using the *fmincon* solver in Matlab in the parameter space (Sp_0, a, b, c) with the constraint of positivity: $\mathrm{Sp}_0 > 0, A^*(s) > 0$ for any $s \in [0, 1]$.

We introduce a theorem [58] of positivity of cubic polynomials on a given interval which states that the polynomial $as^3 + bs^2 + cs + 1$ is nonnegative for all $s \in [0, 1]$ if and only if $(m, n, p, q) \in M \cup N$, where

$$\begin{cases} M = \{(m, n, p, q) : m \geq 0, n \geq 0, p \geq 0, q \geq 0\}, \\ N = \left\{(m, n, p, q) : m \geq 0, q \geq 0, 4mp^3 + 4qn^3 + 27m^2q^2 - 18mnpq - n^2p^2 \geq 0\right\}. \end{cases}$$

and $m = a + b + c + 1, n = b + 2c + 3, p = c + 3, q = 1$. Now, we have the constraints expressed only in terms of the optimization parameters (a, b, c).

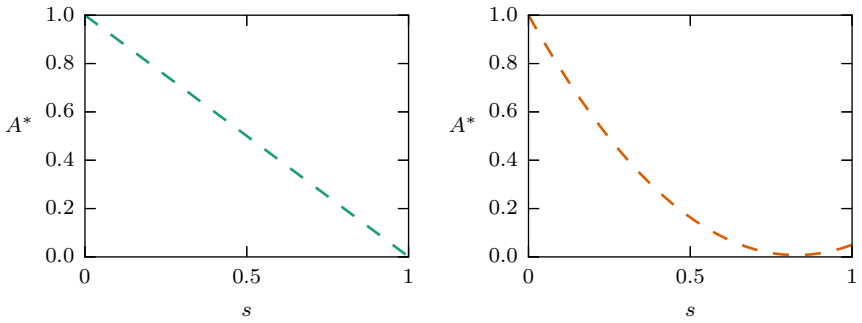

Figure 3.8: (a) Optimal linear stiffness distribution, $\mathrm{Sp}_0 \approx 1.77$. (b) Optimal quadratic stiffness distribution denoted by the dashed line ($\mathrm{Sp}_0 \approx 1.51, F_{\mathrm{p}}^{(2)} \approx 0.2224$)

Fig. 3.8 shows the optimal linear and quadratic stiffness distributions. Both cases reveal a less flexible material at the actuation end ($s = 0$). For example, the optimal linear profile has a basal sperm number $\mathrm{Sp}_0 \approx 1.77$ and the scaled stiffness A^* decreases as s increases. An optimal linear profile improves the propulsive performance by 3% compared with the maximum of the uniform case. The optimal quadratic profile improves the performance by 13% compared with the optimal uniform case. The optimal cubic distribution (not shown in Fig. 3.8)only slightly improves upon the optimal quadratic case.

We note that from a numerical optimization over an exponentially increasing profile, *i.e.*, $A^* = \exp(as), a \geq 0$, the result would be that of the optimal uniform stiffness with $a \approx 0, \mathrm{Sp}_0 \approx 1.89$. This reduction to a uniform distribution indicates that if you start with an optimal uniform stiffness, increasing it down along the body would diminish propulsive performance. On the other hand, the optimal exponentially decreasing stiffness profile ($\mathrm{Sp}_0 \approx 0.1, a \approx -20$) improves the propulsion by 13.5% as compared to the maximum of a filament with uniform

stiffness, which is slightly better than the optimal quadratic distribution.

3.6 Effect of boundary conditions

We have shown that, different from the high Reynolds number case, the torsional spring does not outperform the maximum propulsion achievable by a filament with uniform stiffness under a displacement-driven actuation at the cantilevered extremity of the filament. In general, we observe a trend where a decreasing in stiffness can potentially enhance the propulsive performance of a filament. This result seems to be consistent with the experimental observations obtained by Maier *et. al.* [48] where they found that an exponentially decaying stiffness profile can outperform a filament of uniform stiffness under a rotational actuation. In this section, by considering a torque-free displacement actuation and an angle-driven actuation, we shall show that boundary conditions qualitatively affect the optimality of flexibility. As a result, one cannot simply extend the results by Maier *et. al.* [48] to other situations of propulsion where the actuation techniques may differ.

3.6.1 Torque-free displacement oscillation

We consider a boundary driven passive filament where one end is under torque-free harmonic oscillation while the other end is free [51]. At the actuation end ($s = 0$), we have

$$y(0,t) = y_0 \sin \omega t,\ T_{\text{ext}}(0) = -[A\kappa]_{s=0} = 0, \tag{3.47}$$

After non-dimensionalization, we have $y(0,t) = \epsilon \sin t$ and $\psi_s(0,t) = 0$ where $\epsilon = y_0/L$ is the oscillation amplitude.

Following the cantilevered case, we investigate an elastic-elastic filament at small oscillation amplitude. The governing equations for $\psi_1^{(1)}$ and $\psi_2^{(1)}$ are the same as those obtained for a cantilevered filament, but with different boundary conditions. Once the deforming shape is obtained, the leading order propulsive force is then given by

$$F_{\text{p}}^{(2)} = \frac{1-\gamma}{\gamma \text{Sp}_1^4} \left\langle \psi_1^{(1)}(0,t)\partial_s^2 \psi_1^{(1)}(0,t) + \frac{1}{2}\left[(\partial_s \psi_1^{(1)}(\alpha,t))^2 - \beta(\partial_s \psi_2^{(1)}(\alpha,t))^2\right] \right\rangle. \tag{3.48}$$

For the classical case of uniform bending stiffness along the filament, the variation of propulsive force as a function of the sperm number is shown in Fig. 3.9(a) [4]. For the two values of stiffness chosen according to the blue dots in Fig. 3.9(a), varying the relative proportion of the two segments leads to a non-monotonic variation of the propulsive force (Fig. 3.9(b)). The limits $\alpha = 0, 1$ reduce to the case of uniform stiffness with a propulsive force $F_{\text{p}}^{(2)} = 0.09$ as indicated by the horizontal dash-dotted line in Fig. 3.9(b). By putting a more flexible material at the actuation end *i.e.* $\beta > 1$ (e.g. $\beta = 4.17$, dashed line, Fig. 3.9(b)), the propulsive force generated by such an arrangement can be greater than the maximum possible propulsive

thrust (indicated by the horizontal dotted line in Fig. 3.9(b)) achievable by a filament with *any* uniform bending stiffness. We remark that the proper choice of α is essential because one can obtain a lower propulsion by putting a more flexible material at the driven end. As an example, for $\beta = 4.17$, $\alpha \gtrsim 0.55$, the propulsion achieved using a two-segment filament is worse than the original uniform profile. The aforementioned enhancement in propulsion indicates that the filament prefers to have a more flexible part at the actuation end with an optimal choice of α.

It is interesting to note that these behaviors are qualitatively different from those observed for a displacement-driven cantilevered filament (recall that more flexible material at the driven end is suboptimal in the cantilevered case).

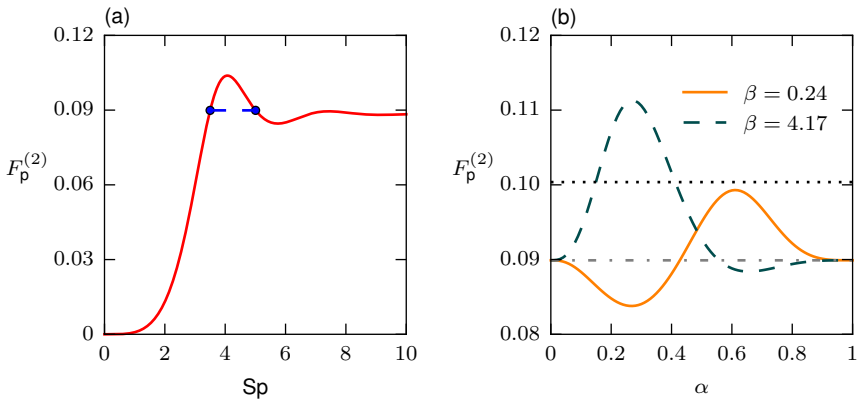

Figure 3.9: (a) Propulsive thrust generated by a filament of uniform bending stiffness actuated at one end [4]. The two blue dots indicate two filaments with different bending stiffnesses generating the same propulsive force. Propulsive thrust generated by two-segment filaments as a function of α at different values of stiffness ratio β. For $\beta = 4.17$ ($A_2 > A_1$, more flexible materials at the actuation end), the maximum propulsive force generated is greater than the maximum achievable thrust of a filament with any uniform stiffness.

3.6.2 Angle oscillation

For an angle oscillation, we may write the dimensionless boundary actuation as $\psi(0,t) = \epsilon \cos t$, $\mathbf{x}(0,t) = \mathbf{0}$ [51, 57]. The method of solutions are similar to those presented in Sec. 3.3 with different boundary conditions which are detailed in Appendix C. For a filament with uniform stiffness, the optimal propulsive performance can be achieved around Sp ≈ 1.88, see Fig. 3.10(a). Similar to the displacement actuation of a cantilevered filament, an elastic-rigid filament under angle actuation cannot outperform the optimum propulsion achievable by a filament with uniform stiffness. In fact, by doing a two parameter (Sp_0, a) numerical optimization over an exponentially increasing stiffness profile, namely $A^* = \exp(as), a \geq 0$, we found that the optimum converges to the maximum of a uniform stiffness with $\mathrm{Sp}_0 \approx 1.88, a \approx 0$. This indicates that if you starts with an optimum uniform stiffness, increasing the stiffness along the body diminishes your performance.

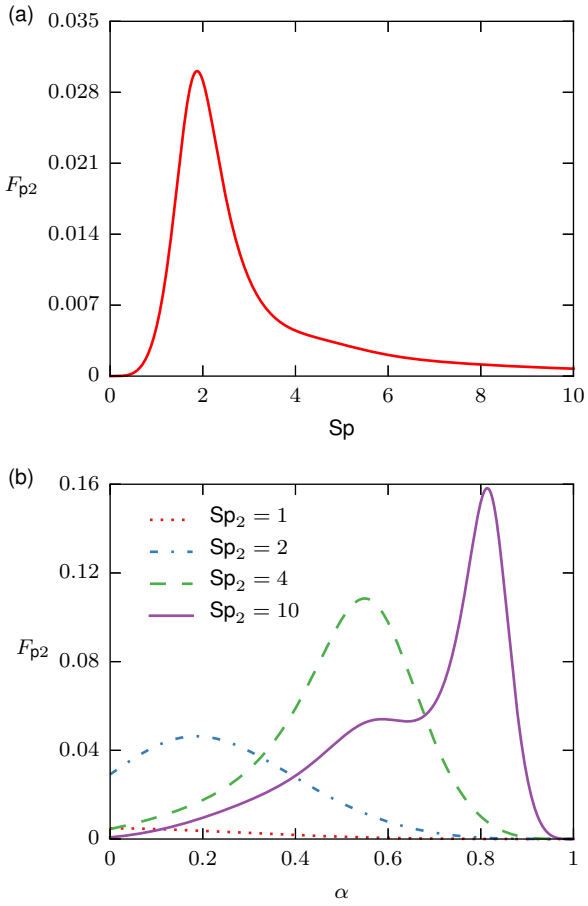

Figure 3.10: (a) Propulsive thrust generated by a filament of uniform bending stiffness with one end under angle oscillation [57]. (b) Propulsive thrust generated by a rigid-elastic filament ($A_1 = \infty$) as a function of α for different sperm numbers (Sp_2) of the flexible part.

On the other hand, the rigid-elastic arrangement can significantly improve the propulsion compared with the uniform case as shown in Fig. 3.10(b) where the leading order propulsive force is plotted as a function of the relative proportion of the rigid segment for several sperm numbers of the flexible part. Take $\mathrm{Sp}_2 = 10$ as an example, the optimum propulsion this arrangement can achieve is one magnitude larger than the maximum of the uniform case. For a rigid-elastic filament, the flexible part is effectively driven by a displacement (rather than an angle oscillation) of the connecting point ($s = \alpha$) though the rigid segment does not contribute to the propulsion. As the length of the flexible part, which contributes to propulsion, decreases (α increases), the displacement of the connecting point increases which tends to enhance the performance. A competition between these two factors yields an optimal α for a given sperm number of the flexible part.

In summary, we've shown that though both elastic-rigid and rigid-elastic cannot outperform the maximum of a uniform case for a displacement-driven cantilevered filament, the rigid-elastic

actually can enhance the propulsive performance for an angle-driven filament.

3.7 Conclusion

In this Chapter, we have presented an analytical and numerical treatment of the optimal propulsive performance of a boundary-driven passive cantilevered filament with variable stiffness along the body in the small amplitude oscillation limit. This work differs from and improves upon previous studies by allowing a varying stiffness profile along the filament. In particular, for the displacement-driven cantilevered filament, we show that different from the high Reynolds number case, the torsional spring arrangement does not enhance the propulsion as compared to an optimal filament with uniform stiffness. However, an exponentially decreasing stiffness profile can improve the propulsion. The rich behavior, particularly the enhancement of propulsion, revealed by our study may be useful for the development of efficient synthetic micro-propellers that can swim as fast as, if not outperform microorganisms nature can offer.

To conclude, we have shown that boundary conditions can qualitatively modify the optimal flexibility arrangement of a driven filament. Therefore, the optimal flexibility distribution may vary from case to case and one may not extend the results obtained from one case to other problems of propulsion where the method of actuation might differ.

Chapter 4

Nonlinear dynamics of a driven microfilament in a viscous fluid

4.1 Introduction

In Chapter 3, we studied the dynamics and propulsion of a boundary driven microfilament in a viscous fluid in the small oscillation amplitude regime ($\epsilon \ll 1$). For small amplitude, the fully nonlinear governing equations are linearized thus makes the dynamics analytically tractable. In this Chapter, we explore the fully nonlinear dynamics by solving the governing equations numerically for amplitudes that are not necessarily small.

4.2 Mathematical formulation

The governing equation for $\mathbf{x}(s,t)$ as derived in Chapter 3 can be given by

$$\xi_\perp \mathbf{x}_t = -(A\mathbf{x}_{ss})_{ss} + (\gamma-1)\mathbf{x}_s\left(2A_s\mathbf{x}_{ss}\cdot\mathbf{x}_{ss} + 3A\mathbf{x}_{sss}\cdot\mathbf{x}_{ss}\right) + \gamma\sigma_s\mathbf{x}_s + \sigma\mathbf{x}_{ss}. \tag{4.1}$$

Differentiating Eq. (4.1) with respect to s and taking a dot product with $\mathbf{x}_s$, we obtain an auxiliary PDE for the Lagrange multiplier $\sigma(s,t)$:

$$\gamma\sigma_{ss} + (\mathbf{x}_s\cdot\mathbf{x}_{sss})\sigma = \mathbf{x}_s\cdot(A\mathbf{x}_{ss})_{sss} - (\gamma-1)(2A_s\mathbf{x}_{ss}\cdot\mathbf{x}_{ss} + 3A\mathbf{x}_{sss}\cdot\mathbf{x}_{ss})_s. \tag{4.2}$$

In order to simplify the above Equation, we successively differentiate the identity $\mathbf{x}_s\cdot\mathbf{x}_s = 1$ and obtain

$$\mathbf{x}_s\cdot\mathbf{x}_{ss} = 0, \tag{4.3}$$

$$\mathbf{x}_{sss}\cdot\mathbf{x}_s + \mathbf{x}_{ss}\cdot\mathbf{x}_{ss} = 0, \tag{4.4}$$

$$\mathbf{x}_{ssss}\cdot\mathbf{x}_s + 3\mathbf{x}_{sss}\cdot\mathbf{x}_{ss} = 0, \tag{4.5}$$

$$\mathbf{x}_{sssss}\cdot\mathbf{x}_s + 4\mathbf{x}_{ssss}\cdot\mathbf{x}_{ss} + 3\mathbf{x}_{sss}\cdot\mathbf{x}_{sss} = 0. \tag{4.6}$$

Using the above identities, we obtain

$$\begin{aligned}\gamma\sigma_{ss} - (\mathbf{x}_{ss}\cdot\mathbf{x}_{ss})\sigma =& -(1+2\gamma)A_{ss}\mathbf{x}_{ss}\cdot\mathbf{x}_{ss} - (2+7\gamma)A_s\mathbf{x}_{ss}\cdot\mathbf{x}_{sss} \\ & - 3\gamma A\mathbf{x}_{sss}\cdot\mathbf{x}_{sss} - (1+3\gamma)A\mathbf{x}_{ss}\cdot\mathbf{x}_{ssss}.\end{aligned} \tag{4.7}$$

We non-dimensionalize the governing equations with respect to a time scale ω^{-1}, length scale L and a force scale $L^2\xi_\perp\omega$. The resulting dimensionless equations are given by

$$\begin{aligned}\mathrm{Sp}^4\mathbf{x}_t =& -(A^*\mathbf{x}_{ss})_{ss} + (\gamma-1)\mathbf{x}_s\left(2A^*_s\mathbf{x}_{ss}\cdot\mathbf{x}_{ss} - A^*\mathbf{x}_s\cdot\mathbf{x}_{ssss}\right) \\ & + \mathrm{Sp}^4\gamma\sigma_s\mathbf{x}_s + \mathrm{Sp}^4\sigma\mathbf{x}_{ss},\end{aligned} \tag{4.8}$$

$$\begin{aligned}\mathrm{Sp}^4\left[\gamma\sigma_{ss} - (\mathbf{x}_{ss}\cdot\mathbf{x}_{ss})\sigma\right] =& -(1+2\gamma)A^*_{ss}\mathbf{x}_{ss}\cdot\mathbf{x}_{ss} - (2+7\gamma)A^*_s\mathbf{x}_{ss}\cdot\mathbf{x}_{sss} \\ & - 3\gamma A^*\mathbf{x}_{sss}\cdot\mathbf{x}_{sss} - (1+3\gamma)A^*\mathbf{x}_{ss}\cdot\mathbf{x}_{ssss},\end{aligned} \tag{4.9}$$

where the same symbols as the dimensional ones are used and $A^*(s) = A(s)/A_0$ and $\mathrm{Sp} = L(\xi_\perp\omega/A_0)^{1/4}$ is the sperm number evaluated using the stiffness at the basal end $s = 0$.

The dimensionless boundary conditions at the free end are given by

$$\sigma\mathbf{x}_s - \mathrm{Sp}^{-4}(A^*\mathbf{x}_{ss})_s = \mathbf{0}, \quad A^*\mathbf{x}_{ss} = \mathbf{0} \tag{4.10}$$

The boundary conditions at the driven end $s = 0$ depends on the mechanisms of actuation. For a torque free displacement oscillation, we may write

$$x(0,t) = 0, \quad y(0,t) = \epsilon\sin t, \quad \mathbf{x}_{ss}(0,t) = \mathbf{0}, \tag{4.11}$$

where $\epsilon = y_0/L$ is the oscillation amplitude which is not necessarily small. For an angle oscillation, we can express the boundary conditions as

$$\psi(0,t) = \epsilon\cos t, \quad \mathbf{x}(0,t) = \mathbf{0}. \tag{4.12}$$

We note that for $A^*(s) \equiv 1$, the governing equations reduce to the case of a filament with uniform stiffness as given by previous work [59].

4.3 Numerical implementation

To solve the equations of motion numerically, we implement a finite difference formulation that combines two different methods suggested by Tornberg and Shelley [60] and Montenegro-Johnson [61]. In our approach, we treat Eq. (4.8) with a multi-step finite difference in time. In

order to derive the numerical method, we write Eq. (4.8) symbolically as

$$\mathbf{x}_t = \mathbf{F}\left(\mathbf{x}_s, \mathbf{x}_{ss}, \mathbf{x}_{sss}, \mathbf{x}_{ssss}; \sigma, \sigma_s\right) \tag{4.13}$$

Now, the finite difference equation is given by

$$\frac{3\mathbf{x}^{n+1} - 4\mathbf{x}^n + \mathbf{x}^{n-1}}{2\Delta t} = \mathbf{F}^{n+1}, \tag{4.14}$$

where Δt is the time step, and $t^n = n\Delta t$. Note that both linear and nonlinear terms in $\mathbf{F}^{n+1}$ are treated *implicitly*. In order to solve the nonlinear finite difference equation at t^{n+1}, we use an iterative approach where at each iteration the implicit terms are linearized as

$$-\mathrm{Sp}^{-4}(A^*\mathbf{x}_{ss})_{ss} + \mathrm{Sp}^{-4}(\gamma-1)\tilde{\mathbf{x}}_s\left(2A^*_s\tilde{\mathbf{x}}_{ss}\cdot\mathbf{x}_{ss} - A^*\tilde{\mathbf{x}}_s\cdot\mathbf{x}_{ssss}\right) + \gamma\sigma_s\tilde{\mathbf{x}}_s + \sigma\tilde{\mathbf{x}}_{ss}, \tag{4.15}$$

where variables with tildes indicate values taken from the previous iteration. At the first iteration of each time step, an extrapolation of the values from previous two time steps ($2\mathbf{x}^n - \mathbf{x}^{n-1}$) are used as initial guess. Similarly for the auxiliary equation for tension at t^{n+1}, we have

$$\begin{aligned}\mathrm{Sp}^4\left[\gamma\sigma_{ss} - (\tilde{\mathbf{x}}_{ss}\cdot\tilde{\mathbf{x}}_{ss})\sigma\right] = &-(1+2\gamma)A^*_{ss}\tilde{\mathbf{x}}_{ss}\cdot\mathbf{x}_{ss} - (2+7\gamma)A^*_s\tilde{\mathbf{x}}_{ss}\cdot\mathbf{x}_{sss}\\ &- 3\gamma A^*\tilde{\mathbf{x}}_{sss}\cdot\mathbf{x}_{sss} - (1+3\gamma)A^*\tilde{\mathbf{x}}_{ss}\cdot\mathbf{x}_{ssss}\\ &+ \lambda(1-\tilde{\mathbf{x}}_s\cdot\mathbf{x}_s),\end{aligned} \tag{4.16}$$

where the term $\lambda(1-\tilde{\mathbf{x}}_s\cdot\mathbf{x}_s)$ is introduced to penalize any length error that might arise from the numerical approach with λ being the penalty factor. The filament is uniformly discretized into N segments ($h = 1/N$) with the nodes (starting from $s = 0$) denoted as $s_j = jh, j = 0, 1, ..., N$. Second order accurate centered finite differences as given by Tornberg and Shelley [60] are used for spatial derivatives in s.

At each iteration in a time step, we solve a linear system of $3(N+1)$ equations to obtain the discrete values of the shape $\mathbf{x}(s_j, t^{n+1})$ and Lagrange multiplier $\sigma(s_j, t^{n+1})$ simultaneously. In general, we terminate the iteration when the relative error of $\mathbf{x}$ in two successive iterations is within 0.5%. To implement the boundary conditions, one-sided finite differences are used.

4.4 Uniform stiffness

For the simple case of a filament with uniform stiffness $A^* \equiv 1$, all the terms that have derivatives of $A^*(s)$ vanish. In Fig. 4.1, we plot the shapes of the deforming filament at different times in one period obtained from linear theory (as given in Chapter 3) along with numerical simulations from the fully nonlinear theory for amplitude $\epsilon = 0.1$ under a torque free displacement oscillation. As can be seen from Fig. 4.1, the numerical solution matches very well with those from the small amplitude asymptotic expansion.

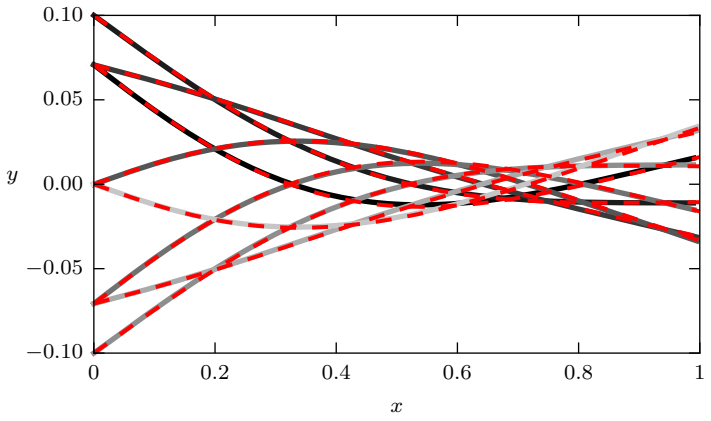

Figure 4.1: Shape (not to scale) of a deforming filament with uniform stiffness Sp = 4 at $\epsilon = 0.1$ at different times $n\pi/4$, where $n = 1, 2, ..., 8$, the intensity of color decreases as time increases. The numerical solution is calculated with $N = 160$ and $\Delta t = 5 \times 10^{-4}$. The red dashed lines denote the shapes obtained from the small amplitude linear theory [4]. The shape from numerical simulation matches very well with those from the small amplitude asymptotic expansion.

In Fig. 4.2, we show the shapes of a deforming filament at different times over one period of the actuation for $\epsilon = 1$ and Sp = 4. It is interesting to note that, different from the linear theory where the waveforms are always symmetric (see Fig. 4.1), complex beating patterns emerge from the intrinsically symmetric model for large amplitude. These asymmetries in waveforms are due to buckling instability followed by complex shape perturbations [59, 62].

From our preliminary results, we've shown that the nonlinear model predicts that the compression of the filament due to the internal forces leads to a transition to symmetry breaking, as well as the breakdown of the small amplitude linear theory. In future study, we want to look at the effect of non-uniform stiffness on the beating pattern for large amplitude oscillation and also the swimming characteristics by allowing the filament to swim freely under a proper actuation.

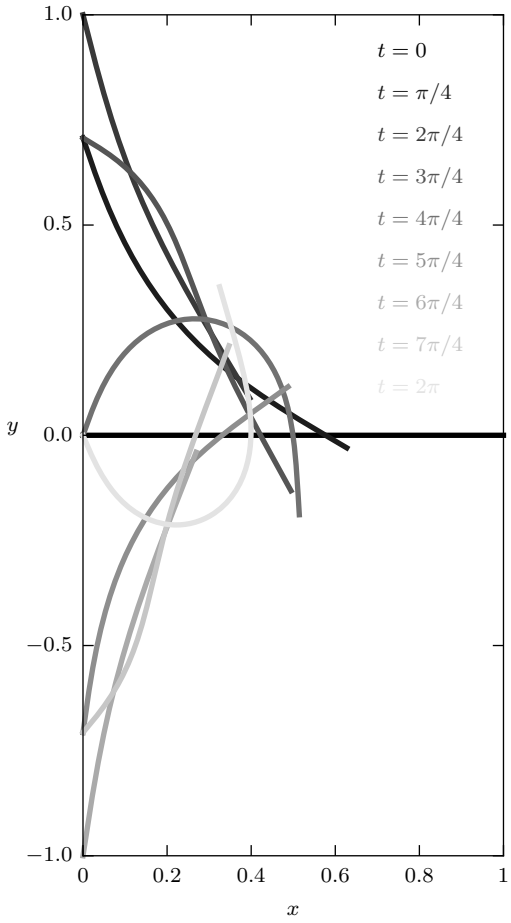

Figure 4.2: Shape of a deforming filament with uniform stiffness $\mathrm{Sp} = 4$ at $\epsilon = 1$ at different times $n\pi/4$, where $n = 0, 1, 2, ..., 8$, the intensity of color decreases as time increases. The solution is calculated with $N = 160$ and $\Delta t = 5 \times 10^{-4}$. Pronounced buckling is observed.

Bibliography

[1] Andrew A Biewener. *Animal locomotion*. Oxford University Press, 2003.

[2] Lisa J Fauci and Robert Dillon. Biofluidmechanics of reproduction. *Annu. Rev. Fluid Mech.*, 38:371–394, 2006.

[3] Eric Lauga and Thomas R Powers. The hydrodynamics of swimming microorganisms. *Rep. Prog. Phys.*, 72(9):096601, 2009.

[4] On Shun Pak and Eric Lauga. Theoretical models in low-Reynolds-number locomotion. In Camille Duprat and Howard A. Stone, editors, *Fluid-Structure Interactions in Low-Reynolds-Number Flows*. Royal Society of Chemistry, 2014.

[5] Edward M Purcell. Life at low Reynolds number. *Am. J. Phys*, 45(1):3–11, 1977.

[6] Christopher Brennen and Howard Winet. Fluid mechanics of propulsion by cilia and flagella. *Annu. Rev. Fluid Mech.*, 9(1):339–398, 1977.

[7] Howard C Berg. *E. coli in Motion*. Springer Science & Business Media, 2008.

[8] J Gray and GJ Hancock. The propulsion of sea-urchin spermatozoa. *J. Exp. Biol.*, 32(4): 802–814, 1955.

[9] James Lighthill. Flagellar hydrodynamics. *SIAM Rev.*, 18(2):161–230, 1976.

[10] J Gray. Undulatory propulsion. *Q. J. Microsc. Sci.*, 3(28):551–578, 1953.

[11] Netta Cohen and Jordan H Boyle. Swimming at low Reynolds number: a beginners guide to undulatory locomotion. *Contemp. Phys.*, 51(2):103–123, 2010.

[12] AT Chwang and TY Wu. A note on the helical movement of micro-organisms. *Proc. R. Soc. B*, 178(1052):327–346, 1971.

[13] Joseph B Keller and SI Rubinow. Swimming of flagellated microorganisms. *Biophys. J.*, 16(2 Pt 1):151, 1976.

[14] JJL Higdon. A hydrodynamic analysis of flagellar propulsion. *J. Fluid Mech.*, 90(04): 685–711, 1979.

[15] J Gray. The mechanism of locomotion in snakes. *J. Exp. Biol.*, 23(2):101–120, 1946.

[16] ZV Guo and L Mahadevan. Limbless undulatory propulsion on land. *Proc. Natl. Acad. Sci. USA*, 105(9):3179–3184, 2008.

[17] David L. Hu, Jasmine Nirody, Terri Scott, and Michael J. Shelley. The mechanics of slithering locomotion. *Proc. Natl. Acad. Sci. USA*, 106(25):10081–10085, 2009. doi: 10.1073/pnas.0812533106.

[18] Silas Alben. Optimizing snake locomotion in the plane. *Proc. R. Soc. A*, 469(2159), 2013. ISSN 1364-5021.

[19] Werner Baumgartner, Florian Fidler, Agnes Weth, Martin Habbecke, Peter Jakob, Christoph Butenweg, and Wolfgang Böhme. Investigating the locomotion of the sandfish in desert sand using nmr-imaging. *PloS One*, 3(10):e3309, 2008.

[20] Ryan D Maladen, Yang Ding, Chen Li, and Daniel I Goldman. Undulatory swimming in sand: subsurface locomotion of the sandfish lizard. *Science*, 325(5938):314–318, 2009.

[21] Yang Ding, Sarah S Sharpe, Andrew Masse, and Daniel I Goldman. Mechanics of undulatory swimming in a frictional fluid. *PLoS Comput. Biol.*, 8(12):e1002810, 2012.

[22] Brian J Williams, Sandeep V Anand, Jagannathan Rajagopalan, and M Taher A Saif. A self-propelled biohybrid swimmer at low Reynolds number. *Nat. Commun.*, 5, 2014.

[23] Ryan D Maladen, Yang Ding, Paul B Umbanhowar, and Daniel I Goldman. Undulatory swimming in sand: experimental and simulation studies of a robotic sandfish. *Int. J. Robot. Res.*, 30(7):793–805, 2011.

[24] M. Sauzade, G. J. Elfring, and E. Lauga. Taylor's swimming sheet: Analysis and improvement of the perturbation series. *Phys. D*, 240:1567 – 1573, 2011.

[25] Tingnan Zhang and Daniel I. Goldman. The effectiveness of resistive force theory in granular locomotiona). *Phys. Fluids*, 26(10):101308, 2014.

[26] Daniel I. Goldman. *Colloquium* : Biophysical principles of undulatory self-propulsion in granular media. *Rev. Mod. Phys.*, 86:943–958, Jul 2014.

[27] R Albert, MA Pfeifer, A-L Barabási, and P Schiffer. Slow drag in a granular medium. *Phys. Rev. Lett.*, 82(1):205, 1999.

[28] Glen Hill, Susan Yeung, and Stephan A Koehler. Scaling vertical drag forces in granular media. *Europhys. Lett.*, 72(1):137, 2005.

[29] Matthias Schröter, Sibylle Nägle, Charles Radin, and Harry L Swinney. Phase transition in a static granular system. *Europhys. Lett.*, 78(4):44004, 2007.

[30] Fuping Zhou, Suresh G. Advani, and Eric D. Wetzel. Simulation of slowly dragging a cylinder through a confined pressurized bed of granular materials using the discrete element method. *Phys. Fluids*, 19(1):013301, 2007.

[31] A. Seguin, Y. Bertho, P. Gondret, and J. Crassous. Dense granular flow around a penetrating object: Experiment and hydrodynamic model. *Phys. Rev. Lett.*, 107:048001, Jul 2011.

[32] Saverio E Spagnolie and Eric Lauga. The optimal elastic flagellum. *Phys. Fluids*, 22(3): 031901, 2010.

[33] BM Friedrich, IH Riedel-Kruse, J Howard, and F Jülicher. High-precision tracking of sperm swimming fine structure provides strong test of resistive force theory. *J. Exp. Biol.*, 213(8):1226–1234, 2010.

[34] Rafael D. Schulman, Matilda Backholm, William S. Ryu, and Kari Dalnoki-Veress. Dynamic force patterns of an undulatory microswimmer. *Phys. Rev. E*, 89:050701, May 2014.

[35] James Lighthill. Mathematical biofluiddynamics. *Society for Industrial & Applied Mathematics, US*, 1975.

[36] Stephen Childress. *Mechanics of swimming and flying*, volume 2. Cambridge University Press, 1981.

[37] Leif E Becker, Stephan A Koehler, and Howard A Stone. On self-propulsion of micromachines at low Reynolds number: Purcell's three-link swimmer. *J. Fluid Mech.*, 490: 15–35, 2003.

[38] Daniel Tam and A. E. Hosoi. Optimal stroke patterns for purcell's three-link swimmer. *Phys. Rev. Lett.*, 98:068105, Feb 2007.

[39] O Pironneau and DF Katz. Optimal swimming of flagellated micro-organisms. *J. Fluid Mech.*, 66(02):391–415, 1974.

[40] Stephan Koehler, Tristan Spoor, and BS Tilley. Pitching, bobbing, and performance metrics for undulating finite-length swimming filaments. *Phys. Fluids*, 24(9):091901, 2012.

[41] RS Berman, O Kenneth, J Sznitman, and AM Leshansky. Undulatory locomotion of finite filaments: lessons from caenorhabditis elegans. *New J. Phys.*, 15(7):075022, 2013.

[42] MJ Lighthill. Hydromechanics of aquatic animal propulsion. *Annu. Rev. Fluid Mech.*, 1 (1):413–446, 1969.

[43] John Young, Simon M. Walker, Richard J. Bomphrey, Graham K. Taylor, and Adrian L. R. Thomas. Details of insect wing design and deformation enhance aerodynamic function and flight efficiency. *Science*, 325(5947):1549–1552, 2009. doi: 10.1126/science.1175928.

[44] Theodore Yaotsu Wu. Fish swimming and bird/insect flight. *Annu. Rev. Fluid Mech.*, 43 (1):25–58, 2011.

[45] Rémi Dreyfus, Jean Baudry, Marcus L Roper, Marc Fermigier, Howard A Stone, and Jérôme Bibette. Microscopic artificial swimmers. *Nature*, 437(7060):862–865, 2005.

[46] On Shun Pak, Wei Gao, Joseph Wang, and Eric Lauga. High-speed propulsion of flexible nanowire motors: Theory and experiments. *Soft Matter*, 7:8169–8181, 2011.

[47] Brian J Williams, Sandeep V Anand, Jagannathan Rajagopalan, and M Taher A Saif. A self-propelled biohybrid swimmer at low reynolds number. *Nat. Commun.*, 5, 2014.

[48] Alexander M. Maier, Cornelius Weig, Peter Oswald, Erwin Frey, Peer Fischer, and Tim Liedl. Magnetic propulsion of microswimmers with dna-based flagellar bundles. *Nano Lett.*, 16(2):906–910, 2016.

[49] Chris H. Wiggins, D. Riveline, A. Ott, and Raymond E. Goldstein. Trapping and wiggling: Elastohydrodynamics of driven microfilaments. *Biophys. J.*, 74(2):1043 – 1060, 1998. ISSN 0006-3495.

[50] Chris H. Wiggins and Raymond E. Goldstein. Flexive and propulsive dynamics of elastica at low reynolds number. *Phys. Rev. Lett.*, 80:3879–3882, Apr 1998.

[51] Arthur A. Evans and Eric Lauga. Propulsion by passive filaments and active flagella near boundaries. *Phys. Rev. E*, 82:041915, Oct 2010.

[52] Hiroto Tanaka, John P Whitney, and Robert J Wood. Effect of flexural and torsional wing flexibility on lift generation in hoverfly flight. *Integr. Comp. Biol.*, 51:142, 2011.

[53] Jialei Song, Haoxiang Luo, and Tyson L Hedrick. Wing-pitching mechanism of hovering ruby-throated hummingbirds. *Bioinspir. Biomim.*, 10(1):016007, 2015.

[54] Kourosh Shoele and Qiang Zhu. Performance of a wing with nonuniform flexibility in hovering flight. *Phys. Fluids*, 25(4):041901, 2013.

[55] M Nicholas J Moore. Torsional spring is the optimal flexibility arrangement for thrust production of a flapping wing. *Phys. Fluids*, 27(9):091701, 2015.

[56] Sébastien Camalet and Frank Jülicher. Generic aspects of axonemal beating. *New J. Phys.*, 2(1):24, 2000.

[57] Tony S. Yu, Eric Lauga, and A. E. Hosoi. Experimental investigations of elastic tail propulsion at low reynolds number. *Phys. Fluids*, 18(9):091701, 2006.

[58] Jochen W Schmidt and Walter Hess. Positivity of cubic polynomials on intervals and positive spline interpolation. *BIT Numerical Mathematics*, 28(2):340–352, 1988.

[59] H Gadêlha, EA Gaffney, DJ Smith, and JC Kirkman-Brown. Nonlinear instability in flagellar dynamics: a novel modulation mechanism in sperm migration? *J. R. Soc. Interface*, page rsif20100136, 2010.

[60] Anna-Karin Tornberg and Michael J Shelley. Simulating the dynamics and interactions of flexible fibers in stokes flows. *Journal of Computational Physics*, 196(1):8–40, 2004.

[61] TD Montenegro-Johnson, Hermes Gadêlha, and David J Smith. Spermatozoa scattering by a microchannel feature: an elastohydrodynamic model. *R. Soc. open Sci.*, 2(3):140475, 2015.

[62] MK Jawed, NK Khouri, F Da, E Grinspun, and PM Reis. Propulsion and instability of a flexible helical rod rotating in a viscous fluid. *Phys. Rev. Lett.*, 115(16):168101, 2015.

Appendix A

Numerical implementation

In this appendix, we present the numerical methods implemented in the optimization of infinite filaments and the solution to the equations of motion of finite length filaments.

A.1 Optimization

The numerical optimization (see Sec. 2.3.1) is performed using MATLAB's built-in *fminsearch* function, which implements the Nelder-Mead simplex algorithm. We truncate the Fourier series by taking $n^* = 100$ to have a sufficient spectral accuracy and use $m = 1000$ points for the Gauss-Legendre integration scheme. Further increase in spectral and spatial resolution has a negligible effect on the optimization. The optimization search routine iterates until the algorithm detects a local solution gradient with a relative error tolerance of 10^{-14}. For each iteration, the swimming speed U is obtained by solving the force balance in the swimming direction using MATLAB's *fzero* function, which runs until a relative error of 10^{-16} is reached. A variety of shapes are provided as the initial guess for the starting of the optimization. The optimization calculation is iterated by taking the converged shape of the previous calculation as the initial guess until the shapes acquired in two successive calculations are consistent. The optimal shape obtained does not vary with the initial guess.

We validate our approach by solving the optimal shape for the Newtonian case. For Newtonian swimming, the swimming speed U can be obtained by a simple matrix inversion due to linearity. The optimal shape obtained from our numerical approach agrees with the analytical solution of Lighthill[35].

A.2 Numerical solution for finite swimmers

The study of swimming characteristics requires solving the force and torque balance of the finite swimmer as formulated in Sec. 2.2. The force- and torque-free conditions posed in Eq. (2.19) and (2.20) provide a system of non-linear ordinary differential equations (ODEs) for the swimmer's linear and angular velocities in terms of its instantaneous location and orientation. The instantaneous velocities in turn, once obtained, can be integrated over time to determine the trajectory, location and orientation of the swimmer.

Having assumed that the centerline of the waveform is initially aligned with the $x-$axis of the lab frame, we solve the swimming problem numerically. Starting at $t = 0$ with a time

step Δt, we denote $t_i = i\Delta t$. With this notation, we employ a second order multi-step finite difference method to discretize the ODEs such that

$$\mathbf{x}_{i+1} = \frac{4}{3}\mathbf{x}_i - \frac{1}{3}\mathbf{x}_{i-1} + \frac{2\Delta t}{3}(2\dot{\mathbf{x}}_i - \dot{\mathbf{x}}_{i-1}). \tag{A.1}$$

We do similarly for θ_{i+1}, and then Θ_{i+1} can be computed. To initialize this numerical scheme, we need both $[\mathbf{x}_0, \theta_0]$ and $[\mathbf{x}_1, \theta_1]$. At the first time step, $[\mathbf{x}_1, \theta_1]$ is computed using the Runge-Kutta fourth order method. At each time step ($i \geq 1$), we obtain $[\dot{\mathbf{x}}_i, \dot{\theta}_i]$ by solving the integral equations for force and torque balance using Gauss-Legendre quadrature integration coupled with MATLAB's *fsolve* routine. We use m points along the filament for the Gauss-Legendre integration method. The *fsolve* routine in Matlab Optimization Toolbox attempts to solve a system of equations by minimizing the sum of squares of all the components. We set the termination tolerance on both the function value and independent variables to 10^{-14}. We generally use $m = 1000$ points along the filament and $T_m = 500$ time steps for one period T of the motion. The number of Fourier modes is taken as $n^* = 100$. Further increasing of the number of spatial points or time steps have no significant influence on the accuracy of the results. All the numerical simulations are performed using MATLAB.

Appendix B

Solution of an elastic-elastic filament

In this section, we derive the solution of an elastic-elastic filament.

B.1 Equations of motion

The dimensionless governing equations are given by

$$\begin{aligned}
&\mathrm{Sp}_1^4\psi_{1t} = -\partial_s^4\psi_1 + \partial_s(\psi_{1s}\tau_1) + \gamma\psi_{1s}\left(\psi_{1s}\partial_s^2\psi_1 + \tau_{1s}\right),\\
&\tau_{1ss} - \frac{1}{\gamma}\psi_{1s}^2\tau_1 = -\partial_s\left(\psi_{1s}\partial_s^2\psi_1\right) - \frac{1}{\gamma}\psi_{1s}\partial_s^3\psi_1,\\
&\mathrm{Sp}_1^4\psi_{2t} = -\beta\partial_s^4\psi_2 + \partial_s(\psi_{2s}\tau_2) + \gamma\psi_{2s}\left(\beta\psi_{2s}\partial_s^2\psi_2 + \tau_{2s}\right),\\
&\tau_{2ss} - \frac{1}{\gamma}\psi_{2s}^2\tau_2 = -\beta\partial_s\left(\psi_{2s}\partial_s^2\psi_2\right) - \beta\frac{1}{\gamma}\psi_{2s}\partial_s^3\psi_2.
\end{aligned} \tag{B.1}$$

The force balance on the entire filament is given by

$$\mathbf{F}_{\mathrm{ext}}(0,t) + \int_0^1 \mathbf{f}_{\mathrm{vis}}\,\mathrm{d}s = \mathbf{0}, \tag{B.2}$$

or

$$-\tau_1\mathbf{t} + \partial_{ss}\psi_1\mathbf{n} = -\int_0^1 \mathbf{f}_{\mathrm{vis}}\,\mathrm{d}s. \tag{B.3}$$

In other words, we have

$$\tau_1(0,t) = \mathbf{t}(0,t)\cdot\int_0^1 \mathbf{f}_{\mathrm{vis}}\,\mathrm{d}s, \tag{B.4}$$

$$\partial_s^2\psi_1(0,t) = -\mathbf{n}(0,t)\cdot\int_0^1 \mathbf{f}_{\mathrm{vis}}\,\mathrm{d}s, \tag{B.5}$$

Since we prescribed the displacement of the point of actuation ($s=0$), we may write

$$\begin{aligned}
\mathbf{x}(0,t) &= [0, \epsilon\sin t]^{\mathsf{T}}\\
&= \mathbf{x}(0,0) + \mathrm{Sp}_1^{-4}\int_0^t \mathrm{d}t\left[\mathbf{n}\left(-\partial_s^3\psi_1 + \psi_{1s}\tau_1\right) + \gamma\mathbf{t}\left(\psi_{1s}\partial_s^2\psi_1 + \tau_{1s}\right)\right]_{s=0}
\end{aligned} \tag{B.6}$$

Differentiating with respect to time, we obtain

$$\begin{aligned} 0 &= -\sin\psi\left(-\partial_s^3\psi_1+\psi_{1s}\tau_1\right)+\gamma\cos\psi\left(\psi_{1s}\partial_s^2\psi_1+\tau_{1s}\right), \\ \epsilon \mathrm{Sp}_1^4\cos t &= \cos\psi\left(-\partial_s^3\psi_1+\psi_{1s}\tau_1\right)+\gamma\sin\psi\left(\psi_{1s}\partial_s^2\psi_1+\tau_{1s}\right). \end{aligned} \tag{B.7}$$

The torque-free condition reads $\psi_{1s}(0,t)=0$. At the free end, we have $\tau_2(1,t)=0, \partial_{ss}\psi_2(1,t)=0, \psi_{2s}(1,t)=0$. At the connecting point, we have $\psi_1(\alpha,t)=\psi_2(\alpha,t), \tau_1(\alpha,t)=\tau_2(\alpha,t), \psi_{1s}(\alpha,t)=\beta\psi_{2s}(\alpha,t), \partial_s^2\psi_1(\alpha,t)=\beta\partial_s^2\psi_2(\alpha,t)$. The last boundary condition is given by the continuity of the viscous force at $s=\alpha$.

At zeroth order, we have $\partial_{ss}\tau_{1,0}=0, \partial_{ss}\tau_{2,0}=0$, which have trivial solutions $\tau_{1,0}(s,t)=\tau_{2,0}(s,t)=0$. At the first order, we also have $\partial_{ss}\tau_{1,1}=0, \partial_{ss}\tau_{2,1}=0$ with zero solutions. This indicates that tension along the filament $\tau\sim\mathcal{O}(\epsilon^2)$, which is consistent with previous studies of uniform stiffness.

Now, expanding the equations for ψ_1 and ψ_2, we have

$$\mathrm{Sp}_1^4\partial_t\psi_1^{(1)}+\partial_s^4\psi_1^{(1)}=0, \quad \mathrm{Sp}_1^4\partial_t\psi_2^{(1)}+\beta\partial_s^4\psi_2^{(1)}=0. \tag{B.8}$$

The corresponding B.C.s at $s=1$ are $\partial_s\psi_2^{(1)}(1,t)=0, \partial_s^2\psi_2^{(1)}(1,t)=0$. By expanding Eq. (B.7), one can show that $\partial_s^3\psi_1^{(1)}(0,t)=-\mathrm{Sp}_1^4\cos t$. The other corresponding B.C.s are given by $\partial_s\psi_1^{(1)}(0,t)=0, \psi_1^{(1)}(\alpha,t)=\psi_2^{(1)}(\alpha,t), \partial_s\psi_1^{(1)}(\alpha,t)=\beta\partial_s\psi_2^{(1)}(\alpha,t), \partial_s^2\psi_1^{(1)}(\alpha,t)=\beta\partial_s^2\psi_2^{(1)}(\alpha,t), \partial_s^3\psi_1^{(1)}(\alpha,t)=\beta\partial_s^3\psi_2^{(1)}(\alpha,t)$.

The PDEs for the local tangent can be reduced to two ODEs,

$$\mathrm{Sp}_1^4 h_1(s)+\partial_s^4 h_1=0, \quad \mathrm{Sp}_1^4 h_1(s)+\beta\partial_s^4 h_1=0, \tag{B.9}$$

with the translated B.C.s given by

$$\begin{aligned} &h_{1s}(0)=0, \quad h_{1sss}(0)=-\mathrm{sp}_1^4, \quad h_{2s}(1)=0, \quad h_{2ss}(1)=0, \quad h_1(\alpha)=h_2(\alpha), \\ &h_{1s}(\alpha)=\beta h_2 s(\alpha), \quad h_{1ss}(\alpha)=\beta h_{2ss}(\alpha), \quad h_{1sss}(\alpha)=\beta h_{2sss}(\alpha). \end{aligned} \tag{B.10}$$

These two ODEs fall into the type so-called hyper-diffusion equations. By assuming a solution of the form $h_1=ce^{ks}$, one can obtain its solution.

B.2 Propulsive force

To leading order, the local tangent vector

$$\mathbf{t}_1\sim\left[0,\epsilon\psi_1^{(1)}(s,t)\right]^{\mathsf{T}}, \quad \mathbf{t}_2\sim\left[0,\epsilon\psi_2^{(1)}(s,t)\right]^{\mathsf{T}}. \tag{B.11}$$

By differentiate $\mathbf{x}(s,t)$ with respect to time in Eq. 3.20, we obtain for the first segment

$$\mathbf{u}_1(s,t) \sim \left[0, \epsilon\cos t + \epsilon\int_0^s \partial_t\psi_1^{(1)}\,\mathrm{d}s\right]^{\mathsf{T}}. \tag{B.12}$$

Similarly for the second segment, we have

$$\mathbf{u}_2(s,t) \sim \left[0, \epsilon\cos t + \epsilon\int_0^\alpha \partial_t\psi_1^{(1)}\,\mathrm{d}s + \epsilon\int_\alpha^s \partial_t\psi_2^{(1)}\,\mathrm{d}s\right]^{\mathsf{T}}. \tag{B.13}$$

Then we have

$$f_{x1} = \mathbf{e}_x\cdot\mathbf{f}_{\mathrm{vis},1} \sim -\epsilon^2\mathrm{Sp}_1^4\left(\frac{1}{\gamma}-1\right)\psi_1^{(1)}\left(\int_0^s \partial_t\psi_1^{(1)}\,\mathrm{d}s + \cos t\right). \tag{B.14}$$

Noting that $\partial_t\psi_1^{(1)} = -\mathrm{Sp}_1^{-4}\partial_s^4\psi_1^{(1)}$, we can calculate the integral and obtain

$$f_{x1} = \left(\frac{1}{\gamma}-1\right)\epsilon^2\psi_1^{(1)}(s,t)\partial_s^3\psi_1^{(1)}(s,t), \tag{B.15}$$

where the boundary term $\partial_s^3\psi_1^{(1)}(0,t) = -\mathrm{Sp}_1^4\cos t$ are used.

Integrating f_{x1} from 0 to α, we have

$$\begin{aligned} F_{x1} = \int_0^\alpha f_{x1}\,\mathrm{d}s \sim \left(\frac{1}{\gamma}-1\right)\epsilon^2\Bigg(&-\frac{1}{2}\partial_s(\psi_1^{(1)})^2(\alpha,t) \\ &+\psi_1^{(1)}(\alpha,t)\partial_s^2\psi_1^{(1)}(\alpha,t) - \psi_1^{(1)}(0,t)\partial_s^2\psi_1^{(1)}(0,t)\Bigg) \end{aligned} \tag{B.16}$$

We do similarly for F_{x2}, and the propulsive force at a given time t is then $F_x \sim F_{x1} + F_{x2}$. Taking the time average of F_x over a period 2π, we obtain the second order propulsive force:

$$F_{\mathrm{p}}^{(2)} = \frac{1-\gamma}{\gamma\mathrm{Sp}_1^4}\left\langle\psi_1^{(1)}(0,t)\partial_s^2\psi_1^{(1)}(0,t) + \frac{1}{2}\left[(\partial_s\psi_1^{(1)}(\alpha,t))^2 - \beta(\partial_s\psi_2^{(1)}(\alpha,t))^2\right]\right\rangle, \tag{B.17}$$

where $\langle ...\rangle = (\int_0^{2\pi}(...)\,\mathrm{d}t)/2\pi$ is the average over one period. We note that terms equate to zero after integration are neglected along the way.

Appendix C

Boundary conditions for angle oscillation

The method of solutions for a two-segment filament under angle oscillation is the same as those in Appendix B, but with different boundary conditions.

For an elastic-elastic filament, the boundary conditions at the connecting point $s = \alpha$ and the free end $s = 1$ are the same as those in Appendix B. However, the boundary conditions at the actuation end is given by

$$\psi_1^{(1)}(0,t) = \cos t, \quad \partial_s^3 \psi_1^{(1)}(0,t) = 0. \tag{C.1}$$

For a rigid-elastic filament, we have $\psi_1 = \psi_1(t)$. The two boundary conditions at the free end are the same as the elastic-elastic case. The boundary conditions at the connecting point are given by

$$\psi_2^{(1)}(\alpha,t) = \cos t, \quad \partial_s^3 \psi_2^{(1)}(\alpha,t) = \alpha \partial_s^4 \psi_2^{(1)}(\alpha,t). \tag{C.2}$$